# Chapter 5
# Blind Experimental Data

All tables and figures of this chapter were published in *Inverse Problems* either in [109] or in [28]. All of them are reprinted with permission. In particular, Tables 5.1–5.5 and 5.6 were published in [109]. Tables 5.6 and 5.7 were published in [28]. Figure 5.1 was published in both [109] and [28]. Figures 5.2a–d, 5.3a, b, 5.4a–d, 5.5a–h and 5.6a–f were published in [109]. Figures 5.7a–c, 5.8a–c, 5.9a–f, 5.10, 5.11, 5.12, 5.13, 5.14a–i and 5.15a, b were published in [28].

## 5.1 Introduction

In this chapter, we demonstrate the performance of the two-stage numerical procedure of Chaps. 2 and 4 for the case of experimental data. Specifically, we present results of publications [28, 109]. Experimental data were collected by Drs. Michael A. Fiddy and John Schenk in a laboratory of The University of North Carolina at Charlotte.

While numerical studies of Chaps. 3 and 4 have confirmed the property number 2 of the informal Definition 1.1.2.1 of the approximate global convergence, results of this chapter confirm the property number 3 of that definition. The first stage of our two-stage numerical procedure was originally applied to the most challenging case of **blind** experimental data [109]. In this chapter, the term "blind" means the following:

1. In each experiment, the coauthors of [109] knew the location of the dielectric inclusion. However, this information was not used in computations, since the approximately globally convergent algorithm of Sect. 2.6.1 does not use such an information.
2. Most importantly, the coauthors of [109], did not know refractive indices of dielectric inclusions. First, the computational results were obtained via the algorithm of Sect. 2.6.1. Next, those refractive indices were measured directly by two independent and well established in physics experimental methods.

L. Beilina and M.V. Klibanov, *Approximate Global Convergence and Adaptivity for Coefficient Inverse Problems*, DOI 10.1007/978-1-4419-7805-9_5,

3. Finally, numerical results were compared with results of those direct measurements.

The comparison of item 3 has revealed that the difference between computed and directly measured refractive indices was only a few percent in six out of six cases. Furthermore, in five out of six cases, this difference was even less than the measurement error of direct measurements; see Tables 5.5 and 5.6 below.

While results of [109] have demonstrated very accurate blind reconstructions results of both locations and refractive indices of dielectric inclusions, their shapes were not imaged well since the latter was outside of the scope of publication [109]. Therefore, the adaptive procedure of the second stage of our two-stage numerical procedure was not applied in [109]. Both stages were applied later to the same experimental data in [28]. The work on [28] was carried out later than one on [109]. Thus, the experimental data were blind only during the work on [109] and were not blind when we have worked on [28]. It was demonstrated in [28] that the two-stage numerical procedure very accurately reconstructs all three components of dielectric inclusions: locations, shapes, and refractive indices.

A simple visual comparison of Fig. 5.3a, b reveals a **huge misfit** between the experimental computationally simulated data. This misfit has caused the main difficulty of the work with experimental data. Indeed, it was unclear what kind of PDE, if any, can describe the highly oscillatory behavior of the measured signal even for the free space case. These oscillations took place regardless on the fact that only one period of the sinusoidal function was used as the shape of the input pulse. Hence, it became clear that standard denoising procedures, for example, Fourier transform, Hilbert transform, spline interpolation, etc., can provide only an insignificant help in our case. As a result, a **radically new** data pre-processing procedure was proposed in [109]. Later, this procedure was complemented by one more step in [28]. This step was necessary for the adaptive stage.

The goal of the data pre-processing is to transform experimental data in such a way which would lead to acceptable boundary conditions for both stages of the two-stage numerical procedure. The idea of data pre-processing is based on the intuition only, and it cannot be justified neither by mathematics nor by physics. The single justification of it is the accuracy of results of reconstructions.

The data processing has likely introduced a large modeling noise. This noise was on the top of the regular measurement noise as well as on the top of the huge misfit between the experimental data and our mathematical model. In addition, we have used only a single hyperbolic PDE (5.1) (the same as (2.1)) for our mathematical model. The Maxwell's system was not used since only a single component of the electric field was measured. Thus, the level of the resulting noise in the boundary data was likely very large and was. Furthermore, the noise level was unknown to the authors of [28, 109]. This is why a very good accuracy of results of [28, 109] is quite surprising. These results are presented in the current chapter.

We remind that our two-stage algorithm does not assume neither any knowledge of the background medium nor any knowledge of the presence/absence of small

"sharp" abnormalities of our interest in the medium. It uses only the knowledge of the target coefficient outside of the medium of interest.

We show in Sect. 5.8.4 that a modified gradient method being applied alone to these experimental data in the "pseudo frequency domain" leads to poor quality results. In other words, a locally convergent algorithm, if taken alone, does not work well for our experimental data. Therefore, the application of the approximately globally convergent method is *crucial* for these data.

## 5.2 The Mathematical Model

We model the process of electric wave field propagation via a single hyperbolic PDE, which is the same as our main PDE (2.1). We use this mathematical model only for our experimental data. Other kinds of experimental data might require different mathematical models. As the forward problem, we consider the following Cauchy problem:

$$\varepsilon_r(x)u_{tt} = \Delta u, \text{ in } \mathbb{R}^3 \times (0,\infty), \tag{5.1}$$

$$u(x,0) = 0,\ u_t(x,0) = \delta(x - x_0). \tag{5.2}$$

Here, $\varepsilon_r(x)$ is the spatially distributed dielectric constant (relative dielectric permittivity),

$$\varepsilon_r(x) = \frac{\varepsilon(x)}{\varepsilon_0},\ \sqrt{\varepsilon_r(x)} = n(x) = \frac{c_0}{c(x)} \geq 1, \tag{5.3}$$

where $\varepsilon_0$ is the dielectric permittivity of the vacuum (which we assume to be the same as the one in the air), $\varepsilon(x)$ is the dielectric permittivity of the medium of interest, $n(x)$ is the refractive index of the medium of interest, $c(x)$ is the speed of the propagation of the EM field in this medium, and $c_0$ is the speed of light in the vacuum, which we assume to be the same as one in the air. We point out that it is the refractive index, which is measured in physics. Dielectric constants are not measured. The assumption $n(x) \geq 1$ means that the speed of the EM field propagation in the medium is less or equal than the one in the air, which is reasonable.

Let $\Omega \subset \mathbb{R}^3$ be a convex bounded domain with the boundary $\partial\Omega \in C^3$. We assume that the coefficient $\varepsilon_r(x)$ of equation (5.1) satisfies the same conditions as ones in (2.3), (2.4):

$$\varepsilon_r(x) \in [1,d],\ \varepsilon_r(x) = 1 \text{ for } x \in \mathbb{R}^3 \setminus \Omega, \tag{5.4}$$

$$\varepsilon_r(x) \in C^3\left(\mathbb{R}^3\right). \tag{5.5}$$

The inequality $\varepsilon_r(x) \geq 1$ follows from (5.3). An upper estimate for the constant $d > 1$ is assumed to be known, although we do not assume that the number $d - 1$ is small. The assumption $\varepsilon_r(x) = 1$ for $x \in \mathbb{R}^3 \setminus \Omega$ means that one has air outside of the medium of interest $\Omega$.

**Coefficient Inverse Problem 5.2.** Suppose that the coefficient $\varepsilon_r(x)$ satisfies (5.4) and (5.5). Assume that the function $\varepsilon_r(x)$is unknown in the domain $\Omega$. Determine the function$\varepsilon_r(x)$ *for* $x \in \Omega$,assuming that the following function $g(x,t)$is known for a single source position $x_0 \notin \overline{\Omega}$:

$$u(x,t) = g(x,t), \forall (x,t) \in \partial\Omega \times (0,\infty). \tag{5.6}$$

The function $g(x,t)$ in (5.6) represents the data for this inverse problem. This function models the data resulting from experimental measurements. Here is a brief outline of the two-step procedure by which we have obtained the function $g(x,t)$:

*Step 1.* First, we have measured the time resolved signal, for a single source location, as it is schematically depicted on Fig. 5.1. The rectangular prism on this figure is a schematic representation of our domain $\Omega$. We have measured this signal only on the lower side of $\Omega$, i.e., on the transmitted side. Hence, we had a very narrow view angle in these measurements. Although it seem to follow from (5.6) that we should also measure the signal on other five sides of the prism $\Omega$, our computational simulations have demonstrated that these sides are much less sensitive to the presence of dielectric abnormalities than the lower side of this prism. Hence, we have not conducted any measurements on those five sides. Instead, we have prescribed to them such boundary values of the function $u := g$ which were calculated via solving the initial boundary value problem (5.11) for $\varepsilon_r \equiv 1$.

*Step 2.* As to the lower side of the rectangular prism $\Omega$, we have applied our data pre-processing procedure to the experimental data collected at this side. Thus, the function, which has resulted from this procedure, is our function $g(x,t)$ on the lower side of $\Omega$.

## 5.3 The Experimental Setup

Below $x$ denotes both a vector $x = (x,y,z) \in \mathbb{R}^3$ and the first component of this vector, where $z$ is the vertical coordinate. It is always clear from the context what is what there. Our source/detectors configuration is schematically depicted on Fig. 5.1. The source has generated an EM wave. Only one component of the vector of the electric field was generated by our source. The same component was measured at the bottom side of the rectangular prism $\Omega$ depicted on Fig. 5.1. Actually, the voltage was measured.

The prism $\Omega$ was our computational domain. It was filled with Styrofoam. Styrofoam is a material, whose dielectric constant $\varepsilon_r \approx 1$, i.e., it is the same as in the air. The sizes of $\Omega$ were $240 \times 140 \times 240$ mm, where "mm" stands for "millimeter."

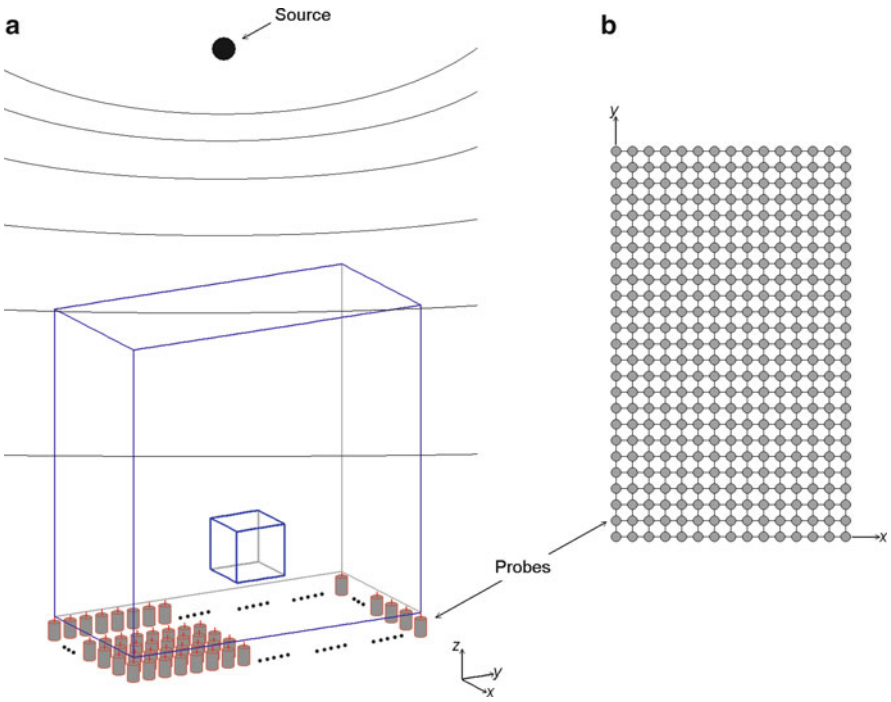


**Fig. 5.1** Schematic diagram of the source/detectors configuration. (**a**) The rectangular prism depicts our computational domain $\Omega$. Only a single-source location outside of this prism was used. Tomographic measurements of the scattered time resolved EM wave were conducted on the bottom side of this prism. (**b**) Schematic diagram of locations of detectors on the bottom side of the prism $\Omega$. The distance between neighboring detectors was 10 mm. Source:M. V. Klibanov, M. A. Fiddy, L. Beilina, N. Pantong and J. Schenk, Picosecond scale experimental verification of a globally convergent numerical method for a coefficient inverse problem, *Inverse Problems*, 26, 045003, doi:10.1088/0266-5611/26/4/045003, 2010. © IOP Publishing. Reprinted with permission

Hence, sizes of front and back sides of the prism of Fig. 5.1 are $240 \times 240$ mm, and sizes of other four sides are $240 \times 140$ mm. The distance between the wave source and the top side of the domain $\Omega$ was 130 mm. The initializing pulse was 100 ps duration. Here, "ps" stands for "picosecond," 1 ps $= 10^{-12}$ s. Since the speed of the EM wave propagation in the air is 0.3 mm/ps, then it requires 433 ps $\approx$ 130/03 ps for this wave to travel from the source to the top boundary of $\Omega$. Hence, it follows from (5.7) that the wave did not yet reach the domain $\Omega$ during the 100 ps duration of this pulse. The initializing pulse was

$$f(\tau) = \begin{cases} \approx A \sin\left(\frac{\pi}{50}\tau\right), \text{ for } \tau \in (0, 100) \text{ ps}, \\ 0, \text{ for } \tau > 100 \text{ ps}, \end{cases} \tag{5.7}$$

where $A > 0$ is the amplitude and $\tau$ is the time in picoseconds. Our data processing procedure does not rely on a knowledge of $A$.

The time resolved signal was measured on a grid on the bottom side of the prism $\Omega$, as indicated on Fig. 5.1b. The grid step size was 10 mm. The detector was moved mechanically from one location to a neighboring one. For each location of the detector, the electric pulse was sent, and one time resolved component of the scattered electric field was measured for the total period of 12,300 ps $=$ 12.3 ns. Hence, it is reasonable to assume in the mathematical model that only one electric pulse was sent and that the wave field was measured simultaneously at all those detectors.

We had two measurements at each detector location. First, we have measured the reference signal when the dielectric inclusion was not present. Actually, this is the case of free space. Next, we have measured the signal when the inclusion was present. In principle, our technique allows the measurement of the reference signal only at a few locations outside of the medium of interest: for the calibration purposes. The only reason why we have measured the reference signal for each location of the detector was that our current numerical implementation works only with the case when the incident wave field is a plane wave. However, it was impossible to arrange a true plane wave in that experiment. In other words, we actually had a spherical wave. On the other hand, using measurements of the reference signal, our data pre-processing procedure has "transformed" this spherical wave into the plane wave.

Although real sizes of the domain $\Omega$ were given above, we have naturally worked with the dimensionless domain. Let $x'$ be the vector of variables with dimensions in millimeters. Then our dimensionless vector was $x = x'/50$ mm. Since the distance between two neighboring detectors was 10 mm, then the dimensionless distance is $\tilde{h} = 10/50$ mm $= 0.2$. Thus, our dimensionless computational domain $\Omega$ and the dimensionless distance $\tilde{h}$ between two neighboring detectors were

$$\Omega = \{(x, y, z) \in [-2.4, 2.4] \times [-1.4, 1.4] \times [-2.4, 2.4]\}, \tilde{h} = 0.2, \ t \in (0, 12). \tag{5.8}$$

Let $P$ be the bottom side of the domain $\Omega$ in (5.8):

$$P = \{(x, y, z) : (x, y) \in [-2.4, 2.4] \times [-1.4, 1.4], \ z = -2.4\}. \tag{5.9}$$

We now explain how we got the dimensionless time. First, about the zero time. We knew that the signal arrives at the detector approximately at 11,520 ps. Since the distance between the planar surface $P$ in (5.9) and the source was 370 mm, the speed of light in the air is 0.3 mm/ps and (370 mm) / (0.3 mm/ps) $=$ 1,233 ps, then the zero time should be at $11,520\,\text{ps} - 1,233\,\text{ps} \approx 10,300\,\text{ps} := \tau_0$. Hence, we should work with a new time variable $\tau' = \tau - \tau_0$. The refractive index outside of the domain $\Omega$ is $n(x) = 1$. Hence, the EM wave should travel the dimensionless distance of $\tilde{h} = 0.2$ between two neighboring detectors in 0.2 dimensionless time units. On the other hand, 0.2 corresponds to the 10 mm distance between two neighboring detectors. Let $t$ denotes the dimensionless time. Then we should choose such a multiplier $\gamma > 0$, which has dimension in picoseconds, that $\gamma t = \tau'$. Hence, we should have

$$0.2\gamma \text{ ps} = \frac{10\,\text{mm}}{0.3\,(\text{mm/ps})},$$

which implies that $\gamma = 166.67\,\text{ps}$. Thus, the dimensionless time $t$ is

$$t = \frac{\tau'}{166.67}.$$

However, the above transformations to dimensionless variables did not affect our governing PDE (5.1) because of the data pre-processing procedure described below in this chapter.

## 5.4 Data Simulations

Since the computationally simulated data play an important role in our data pre-processing procedure, we outline here the solution of the forward problem for equation (5.1). Since it is practically impossible to solve the PDE (5.1) in the entire space $\mathbb{R}^3$, we have solved it in a larger rectangular prism:

$$G = \{(x, y, z) \in [-3, 3] \times [-2, 2] \times [-5, 5]\}.$$

By (5.8), $\Omega \subset G$. Our initializing plane wave in simulations was $v(t)$:

$$v(t) = \begin{cases} \sin(\omega t), \text{ for } t \in \left(0, \frac{2\pi}{\omega}\right), \\ 0, \text{ for } t > \frac{2\pi}{\omega}, \omega = 7. \end{cases} \tag{5.10}$$

Let $\partial G_1$ and $\partial G_2$ be respectively top and bottom sides of $G$ and $\partial G_3 = \partial G \setminus (\partial G_1 \cup \partial G_2)$ be the rest of the boundary of $G$. We have numerically solved the following initial boundary value problem:

$$\begin{aligned} \varepsilon_r(x)\, u_{tt} &= \Delta u, \quad \text{in } G \times (0, T), T = 12, \\ u(x, 0) &= 0,\ u_t(x, 0) = 0, \text{ in } G, \\ \partial_n u\big|_{\partial G_1} &= v(t), \text{ on } \partial G_1 \times (0, 2\pi/\omega], \\ \partial_n u\big|_{\partial G_1} &= -\partial_t u, \text{ on } \partial G_1 \times (t_1, T), \\ \partial_n u\big|_{\partial G_2} &= -\partial_t u, \text{ on } \partial G_2 \times (0, T), \\ \partial_n u\big|_{\partial G_3} &= 0, \text{ on } \partial G_3 \times (0, T). \end{aligned} \tag{5.11}$$

In the case when the data are simulated for the reference medium, we have in (5.11) $\varepsilon_r(x) \equiv 1$. We denote this solution as $u_1(x, t)$. Thus, in (5.11), the plane wave is initialized at the top boundary $\partial G_1$ for times $t \in (0, 2\pi/\omega]$ and propagates

into $G$. First-order absorbing boundary conditions were used on the top boundary for $t \in (2\pi/\omega, T)$ as well as on the bottom boundary $\partial G_2$ for $t \in (0, T)$. The zero Neumann boundary condition was used on the rest of the boundary of the prism $G$. The latter boundary condition is used because the "pure" plane wave with $\varepsilon_r(x) \equiv 1$ satisfies this condition. The problem (5.11) was solved by the hybrid FEM/FDM method. In this method, FDM is used outside of the domain $\Omega$, i.e., in $G \setminus \Omega$, and FEM is used inside $\Omega$. The step size in the overlapping region was $\tilde{h} = 0.2$ which is the same as the distance between any two neighboring detectors.

## 5.5 State and Adjoint Problems for Experimental Data

First, we remind the Tikhonov functional (4.8) of Sect. 4.3. Let $\varepsilon_r^{\text{glob}}(x)$ be the coefficient $\varepsilon_r(x)$ which was reconstructed on the first stage of our two-stage numerical procedure, i.e. when applying the approximately globally convergent algorithm of Sect. 2.6.1. The Tikhonov regularization functional is

$$E_\alpha(\varepsilon_r) = \frac{1}{2}\int\limits_{S_T} (u\mid_{S_T} - g(x,t))^2 z_\xi(t)\,\mathrm{d}S_x\mathrm{d}t + \frac{1}{2}\alpha\int\limits_{\Omega} (\varepsilon_r - \varepsilon_r^{\text{glob}})^2 \mathrm{d}x. \tag{5.12}$$

Our goal now is to find a minimizer $\varepsilon_{r,\alpha}$ of this functional, i.e., to find the *regularized solution*. Let $Y$ be the set of functions defined in (4.7) (Sect. 4.3) and $H_1$ be the finite dimensional space of finite elements constructed in Sect. 4.9.1. We remind that the set $Y_1$ is defined as $Y_1 := Y \cap H_1$. We assume that $\varepsilon_r^{\text{glob}} \in Y_1$ and assume that conditions of Theorems 4.11.1–4.11.4 hold. In particular, these theorems imply existence and uniqueness of the minimizer $\varepsilon_{r,\alpha} \in Y_1$ in a small neighborhood of the exact solution $\varepsilon_r^*$. Thus, below in this section, we work only in that small neighborhood of $\varepsilon_r^*$.

As to state and adjoint problems, although the theory of Chap. 4 works with solutions of those problems only in the domain $Q_T = \Omega \times (0, T)$, we consider in the current chapter different domains for these problems. Still, we believe that the theory of the adaptivity of Chap. 4 can be extended to this case, although we have not yet done this. At this time, however, this difference of domains represents one of discrepancies between the above theory and its numerical implementation. Indeed, if defining solutions of state and adjoint problems like in (4.9) and (4.10) (Sect. 4.3), then, in the case of our experimental data, it is unclear how to figure out the normal derivative $p(x,t) = \partial_n u\mid_{S_T}$ at the lateral boundary $S_T = \partial\Omega \times (0, T)$ of the time cylinder $Q_T$.

Hence, consider the rectangular prism $G' = G \cap \{z > -2.4\}$. Let the rectangle $P_{\text{obs}} = \{z = -2.4\} \cap G$ be the bottom side of $G'$. By (5.9), the rectangle $P \subset P_{\text{obs}}$. Let

$$G_T' = G' \times (0,T),\ S_T' = P_{\text{obs}} \times (0,T),\ S_T'' = \left(\partial G' \setminus P_{\text{obs}}\right) \times (0,T). \tag{5.13}$$

Recall that the lower side $P$ of the rectangular prism $\Omega$ is much more sensitive to experimental data than other five sides of this prism (Sect. 5.2). For this reason, we have prescribed the same data to those five sides as the ones for the case of the free space. Hence, let $u(x,t,\varepsilon_r)$ be the solution of the initial boundary value problem (5.11). Also, let $u_1(x,t)$ be the solution of this problem for $\varepsilon_r(x) \equiv 1$. For the same reason as above, we *approximately* assume that

$$u(x,t,\varepsilon_r) = u_1(x,t) \text{ for } (x,t) \in S''_T. \tag{5.14}$$

Thus, we define state and adjoint problems for our case as:

1. The state problem is the initial boundary value problem (5.11).
2. The adjoint problem is

$$\begin{aligned} \varepsilon_r(x)\lambda_{tt} - \Delta\lambda = 0, \quad (x,t) \in G'_T, \\ \lambda(x,T) = \lambda_t(x,T) = 0, \\ \partial_n\lambda \mid_{S'_T} = (g-u)(x,t), \\ \partial_n\lambda \mid_{S''_T} = 0. \end{aligned} \tag{5.15}$$

The last line of (5.15) follows from (5.14). Similarly with Sects. 4.15.3 and 4.16.2, we have dropped the function $z_\zeta(t)$ in the third line of (5.15), since this function is used only for the compatibility conditions at $t = T$, and we have observed that $u(x,T) \approx g(x,T) \approx 0$ for $x \in \partial G'$. Thus, we have not used the function $z_\zeta(t)$ in (5.12) in our computations of this chapter.

However, since measurements give us (after pre-processing) the function $g(x,t)$ only for $x \in P$, it follows from (5.13) and (5.14) that we should somehow extend this function on the set $P_{\text{obs}} \setminus P$. Hence, we actually need to know the function $g(x,t)$ not only for $x \in P$ but also for $x$ belonging to a wider rectangle $P_{\text{obs}}, x \in P_{\text{obs}}$. In general, this extension problem is very similar with the problem of analytic continuation. And the latter problem is very unstable. However, using some features of our specific arrangement, we have found a different way of this extension via the so-called *third stage* of our data immersing procedure, which is described in Sect. 5.6.

Assuming that the function $g(x,t)$ is properly extended from $P$ into a larger rectangle $P_{\text{obs}}$, the Tikhonov functional (5.12) becomes

$$E_\alpha(\varepsilon_r) = \frac{1}{2}\int\limits_{S'_T} (u \mid_{S'_T} - g(x,t))^2 \mathrm{d}S_x \mathrm{d}t + \frac{1}{2}\alpha \int\limits_{\Omega} (\varepsilon_r - \varepsilon_r^{\text{glob}})^2 \mathrm{d}x. \tag{5.16}$$

Now, we reformulate two mesh refinement recommendations (4.189) and (4.190) of Sect. 4.13.2 for our particular case. Let $\varepsilon_{r,h}(x)$ be the minimizer of the Tikhonov functional (5.12) on the current mesh.

**First Mesh Refinement Recommendation.** *Refine the mesh in such a subdomain of the domain $\Omega$ where*

$$\left|E'_\alpha\left(\varepsilon_{r,h}\right)(x)\right| \geq \beta_1 \max_{\overline{\Omega}} \left|E'_\alpha\left(\varepsilon_{r,h}\right)(x)\right|, \tag{5.17}$$

*where $\beta_1 \in (0,1)$ is the tolerance number and*

$$\left|E'_\alpha\left(\varepsilon_{r,h}\right)(x)\right| = \left|\alpha(\varepsilon_{r,h} - \varepsilon_r^{\text{glob}})(x) - \int_0^T \left(u_{ht}\lambda_{ht}\right)(x,t,\varepsilon_{r,h})\,\mathrm{d}t\right|.$$

*Here, functions $u_{ht}(x,t,\varepsilon_{r,h})$ and $\lambda_{ht}(x,t,\varepsilon_{r,h})$ are solutions of state and adjoint problems, respectively, on the current mesh.*

**The Second Mesh Refinement Recommendation.** *Refine the mesh in such a subdomain of the domain $\Omega$ where*

$$\varepsilon_{r,h}(x) \geq \beta_2 \max_{\overline{\Omega}} \varepsilon_{r,h}(x), \tag{5.18}$$

*where $\beta_2 \in (0,1)$ is the tolerance number.*

Recall that tolerance numbers $\beta_1, \beta_2$ are chosen numerically. In our tests below, we use

$$\beta_1 = 0.8, \beta_2 = 0.2, \alpha = 0.001. \tag{5.19}$$

## 5.6 Data Pre-Processing

The main idea of the data pre-processing procedure is to *immerse* the experimental data in the computationally simulated ones. The data pre-processing procedure provides us with the boundary data at $\partial\Omega$, which we use in our computations. Recall that measurements were not carried out at $\partial\Omega \setminus P$. We have prescribed

$$u(x,t)\mid_{\partial\Omega\setminus P} := u_1(x,t)\mid_{\partial\Omega\setminus P},$$

where $u_1(x,t)$ is the solution of the problem (5.11) with $\varepsilon_r(x) \equiv 1$. So, in this section we describe how we pre-process the data only on the bottom side $P$ of the rectangular prism $\Omega$.

### *5.6.1 The First Stage of Data Immersing*

Samples of unprocessed time resolved experimental data are depicted on Fig. 5.2. We work only with the first burst. Figure 5.2c, d display the curves which are

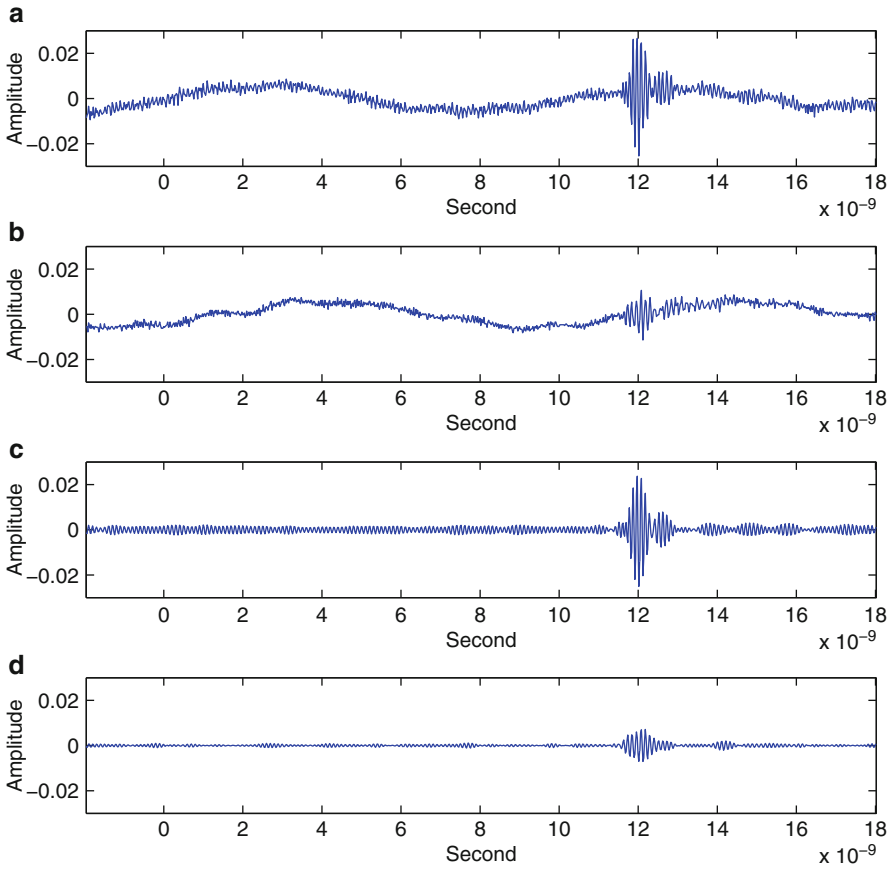


**Fig. 5.2** (**a**) A sample of the measured reference time resolved signal (i.e., no inclusion present) at the location $x_m \in P$ of the probe number $m$. (**b**) The measured signal with inclusion present at the same probe location. The first burst starts when the EM wave arrives at the probe. The signal before this burst reflects a process within the probe itself. (**c**) And (**d**) represent signals (**a**) and (**b**), respectively, after cleaning some noise via applying the fast Fourier transform procedure of MATLAB and truncating too low and too high frequencies. We are interested in the area of the first burst only. One can observe that the amplitude of the signal with the dielectric inclusion present (**d**) is generally less than one of the reference signal. Source: M. V. Klibanov, M. A. Fiddy, L. Beilina, N. Pantong and J. Schenk, Picosecond scale experimental verification of a globally convergent numerical method for a coefficient inverse problem, *Inverse Problems*, 26, 045003, doi:10.1088/0266-5611/26/4/045003, 2010. © IOP Publishing. Reprinted with permission

obtained from curves Fig. 5.2a, b, respectively, after a partial denoising via the Fourier transform. Both Fig. 5.2c, d are for the same detector. Fig. 5.2c is for the case of free space and Fig. 5.2d is for the case when a dielectric inclusion is present. The most troubling feature of Fig. 5.2 is the highly oscillatory behavior of the first burst. Indeed, given that the input data was the sinusoidal function $f(t)$ in (5.7) with

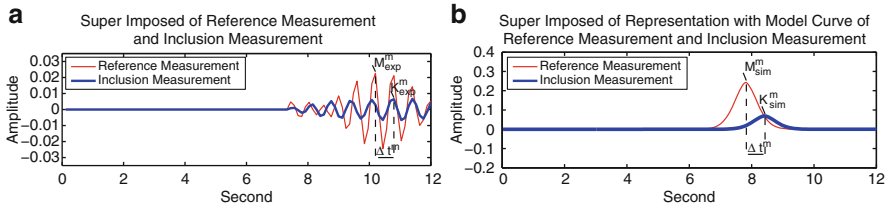


**Fig. 5.3** This figure explains the idea of the first stage of data immersing in the time domain. We have intentionally set to zero the small amplitude fluctuations before that first burst. (**a**) Resulting superimposed experimental curves. The *red curve* (*thin*) is for the reference signal and the *blue curve* (*thick*) is for the signal with a dielectric inclusion present, both at the same location $x_m \in P$ of the detector number $m$. (**b**) The *red curve* (*thin*) displays computationally simulated data $u_1(x_m, t)$. The *blue curve* (*thick*) $u_{\text{incl}}(x_m, t) = u_1(x_m, t - \Delta t^m) K^m_{\text{exp}} / M^m_{\text{exp}}$ represents a sample of the immersed experimental data in the time domain at the same detector location $x_m \in P$. It is only the *blue curve* (*thick*) with which we work further. The *red curve* (*thin*) is displayed for the illustration purpose only. Source: M. V. Klibanov, M. A. Fiddy, L. Beilina, N. Pantong and J. Schenk, Picosecond scale experimental verification of a globally convergent numerical method for a coefficient inverse problem, *Inverse Problems*, 26, 045003, doi:10.1088/0266-5611/26/4/045003, 2010. © IOP Publishing. Reprinted with permission

only one period of the sinusoid, one cannot expect high oscillations of the output signal for, for example, the case of the free space. These oscillations represent the abovementioned huge misfit between experimentally measured and simulated data.

Figure 5.3a displays superimposed Fig. 5.2c, d after their parts prior the first burst was made zero. The thin curve on Fig. 5.3a corresponds to the free space and the thick curve corresponds to the case when the inclusion is present. Let $x_m \in P$ be the detector number $m$ at the bottom side $P$ of the prism $\Omega$; see (5.9) for $P$. We have decided to "immerse" our experimental data in the computationally simulated data using the following two peaks for each detector $x_m$:

1. The largest peak in the thin curve with the peak value of $M^m_{\text{exp}} > 0$.
2. The next peak after it on the thick curve with the peak value of $K^m_{\text{exp}} > 0$. This next peak was chosen because the presence of a dielectric inclusion results in a time delay of the EM wave; see (5.3).

Recall that the function $u_1(x, t)$ is the solution of the problem (5.11) with computationally simulated data for $\varepsilon_r \equiv 1$. Obviously,

$$u_1\left(x^{(1)}, t\right) = u_1\left(x^{(2)}, t\right), \ \forall x^{(1)}, x^{(2)} \in P, \ \forall t \in (0, T).$$

The first peak of the function $u_1(x, t), x \in P$ is the largest peak of Fig. 5.3b. Below $t$ is the *dimensionless* time. Let $t := t^{\text{sim}}_{\text{ref}}$ be the time of the first arrival of the computationally simulated plane wave $u_1(x, t)$ at the plane $P$. In other words, for all $x \in P$, we have $u_1(x, t) = 0$ for $t < t^{\text{sim}}_{\text{ref}}$ and $u_1(x, t) > 0$ for time values $t > t^{\text{sim}}_{\text{ref}}$ that are rather close to $t^{\text{sim}}_{\text{ref}}$; see the reference curve on Fig. 5.3b.

We point out that amplitudes of largest peaks of experimental curves for the reference medium were different for different detectors. This is because we had

in the experiment a spherical incident wave instead of the desired plane wave. Nevertheless, we have "forced" the spherical wave to be a plane wave via applying the first stage of our data immersing procedure.

Let $y = y_m^{\text{ref}}(t)$ be the experimentally measured curve at the detector $\{x_m\}$ for the free space, i.e., this is the thin curve of Fig. 5.3a. Let the above chosen largest peak of this curve is achieved at $\left\{t = t_m^{\text{ref}}\right\}$ and $y_m^{\text{ref}}\left(t_m^{\text{ref}}\right) = M_{\text{exp}}^m > 0$. Let $y = y_m^{\text{incl}}(t)$ be the experimentally measured curve at the detector $\{x_m\}$ for the case when the inclusion is present. We choose such a local maximum of the function $y = y_m^{\text{incl}}(t)$ which is achieved at the first point $\left\{t = t_m^{\text{incl}}\right\}$ which follows after the point $\left\{t = t_m^{\text{ref}}\right\}$; see Fig. 5.3a. Let $y_m^{\text{incl}}\left(t_m^{\text{incl}}\right) = K_{\text{exp}}^m$. Hence, $K_{\text{exp}}^m$ is the value of the latter peak; see Fig. 5.3a. We have observed that $K_{\text{exp}}^m \leq M_{\text{exp}}^m$ on all detectors. This is because the presence of dielectrics decreases the amplitude of the EM wave.

Now, we are ready to immerse our experimental data in the computationally simulated data. Let $\Delta t_m = t_m^{\text{incl}} - t_m^{\text{ref}}$ be the time delay between two above chosen peaks; see Fig. 5.3a. We set

$$u_{\text{incl}}(x_m, t) := \begin{cases} \frac{K_{\text{exp}}^m}{M_{\text{exp}}^m} u_1(x_m, t - \Delta t_m), & \text{if } \frac{K_{\text{exp}}^m}{M_{\text{exp}}^m} < \frac{2}{3}, \\ u_1(x_m, t) \text{ and } \Delta t_m := 0, & \text{if } \frac{K_{\text{exp}}^m}{M_{\text{exp}}^m} \geq \frac{2}{3}. \end{cases} \tag{5.20}$$

Thus, (5.20) is our *first immersed data in the time domain* for the detector number $m$. Figure 5.3b illustrates (5.20). After this data immersing, we use only the curve $u_{\text{incl}}(x_m, t)$ and do not use anymore the curve which corresponds to the reference medium. In other words, on each detector, we use only such curve which corresponds to the thick curve on Fig. 5.3b. We cannot rigorously justify our above decision to work with those peaks only. However, since our results of blind imaging in [109] were very accurate ones, then this justifies our purely intuitive choice.

### 5.6.2 The Second Stage of Data Immersing

Although the thick curve on Fig. 5.3b is smooth, in fact the noise went into the noise with respect to spatial variables on the rectangle $P$, and this will be seen in the current section. We have found that the following frequency interval was the optimal one for our computations:

$$s \in [3.5, 7.5]. \tag{5.21}$$

We apply the Laplace transform (2.10) to each function $u_{\text{incl}}(x_m, t)$ for nine values of $s = 3.5, 4, \ldots, 7.5$ from the interval (5.21). Denote $w_{\text{incl}}(x_m, s)$ the Laplace transform of the function $u_{\text{incl}}(x_m, t)$. Let

$$\tilde{w}_{\text{incl}}(x_m, s) = -\frac{\ln w_{\text{incl}}(x_m, s)}{s^2}.$$

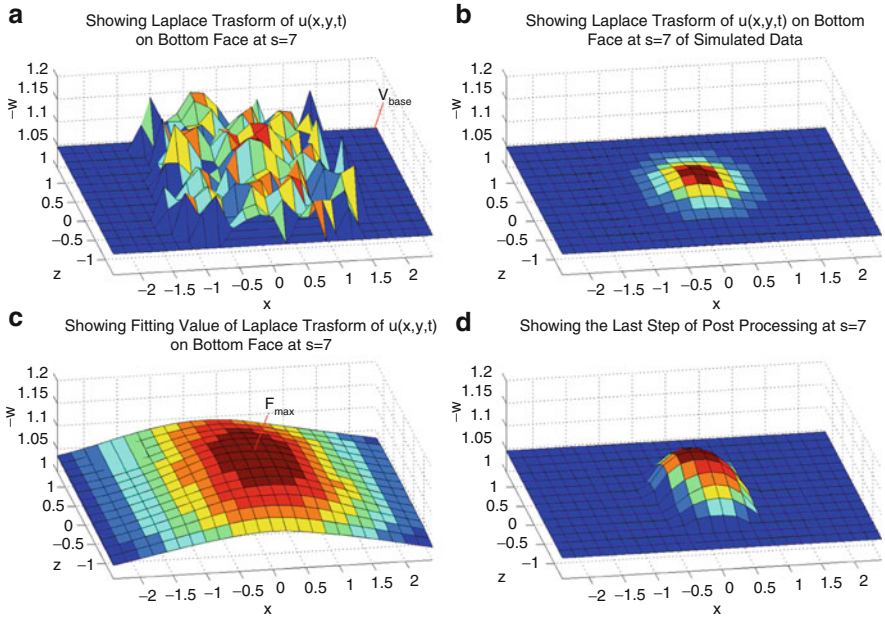


**Fig. 5.4** (**a**) The function $\tilde{w}_{\text{incl}}(x,\overline{s})$, $\overline{s}=7.5$. (**b**) The function $-(\ln w_{\text{sim}}(x,\overline{s}))/\overline{s}^2$is depicted, where $w_{\text{sim}}(x,\overline{s})$is the Laplace transform of the function $u_{\text{sim}}(x,t)$for a computationally simulated data. Figure (**b**) is given only for the sake of comparison with Figure (**a**). (**c**) The function $\tilde{w}_{\text{smooth}}(x,\overline{s})$ resulting from fitting of (**a**) by the lowess fitting procedure in the 2D case; see MATLABR 2009a. (**d**) The final function $\tilde{w}_{\text{immers}}(x,\overline{s})$. Values of $\tilde{w}_{\text{immers}}(x,s)$are used to produce the Dirichlet boundary conditions $\tilde{\psi}_n(x)$for PDEs (2.36) of the globally convergent algorithm. Source: M. V. Klibanov, M. A. Fiddy, L. Beilina, N. Pantong and J. Schenk, Picosecond scale experimental verification of a globally convergent numerical method for a coefficient inverse problem, *Inverse Problems*, 26, 045003, doi:10.1088/0266-5611/26/4/045003, 2010. © IOP Publishing. Reprinted with permission

Let $\overline{w}_{\text{incl}}(x,s)$ be the standard linear interpolation of the values $\{\tilde{w}_{\text{incl}}(x_m,s)\}$ over the plane $P$. We have observed that the function $\overline{w}_{\text{incl}}(x,s)$ is very noisy with respect to $x\in P$. Figure 5.4a displays a sample of the function $\overline{w}_{\text{incl}}(x,\overline{s})$. Hence, the noise went from the time dependence into the spatial dependence.

On the other hand, we have computationally simulated the data with a single inclusion and have obtained the function $w_{\text{sim}}(x,\overline{s})$; see Fig. 5.4b for the function

$$-\frac{\ln w_{\text{sim}}(x,\overline{s})}{s^2}.$$

One can observe that, unlike Fig. 5.4a, b is smooth and has only a single bump. Comparison of Fig. 5.4a, b has motivated us to perform additional procedures with the function $\overline{w}_{\text{incl}}(x,s)$.

Thus, we have applied a smoothing procedure with respect to $(x, y) \in P$ to the function $\overline{w}_{\text{incl}}(x_m, s)$ for each of above nine values of $s$. Specifically, we have used the *Lowess fitting procedure* in the 2D case, which we took from MATLABR 2009. As a result, we have obtained the function $\overline{w}_{\text{smooth}}(x, s)$. The function $\overline{w}_{\text{smooth}}(x, \overline{s})$ is displayed on Fig. 5.4c. Still, comparison of Fig. 5.4b, c tells one that we should transform Fig. 5.4c in such a way which would end up with a single bump. Let $w_1(x, s)$, $x \in P$ be the Laplace transform of the function $u_1(x, t)$, i.e., for the case of the plane wave propagating in the air. Then we finally set for each of those nine values of $s$:

$$\overline{w}_{\text{immers}}(x, s) = \begin{cases} \overline{w}_{\text{smooth}}(x, s), & \text{if } \overline{w}_{\text{smooth}}(x, s) \geq 0.985 \max_{\overline{P}} \overline{w}_{\text{smooth}}(x, s), \\ -s^{-2} \ln w_1(x, s), & \text{otherwise.} \end{cases}$$

Figure 5.4d the function $\overline{w}_{\text{immers}}(x, \overline{s})$, which is obtained from the function $\overline{w}_{\text{incl}}(x, s)$ of Fig. 5.4a.

We use the function $\overline{w}_{\text{immers}}(x, s)$ to obtain Dirichlet boundary conditions for elliptic equations for functions $q_n$ of Sect. 2.6.1. Namely, we use finite differences to approximately compute the $s$-derivative by

$$\psi_n(x) = \frac{\overline{w}_{\text{immers}}(x, s_n - 0.5) - \overline{w}_{\text{immers}}(x, s_n)}{0.5}, \quad x \in P. \tag{5.22}$$

As to the values of the function $\psi_n(x)$ on other five sides of the prism $\Omega$, they were computed by the same finite difference formula using the function resulting from the Laplace transform of the function $u_1(x, t)$.

## 5.7 Some Details of the Numerical Implementation of the Approximately Globally Convergent Algorithm

We point out that all details of the numerical implementation of the approximately globally convergent algorithm, which are described in this section, were implemented a few months before the experimental data were collected. When working with the experimental data, we have not changed neither our original numerical code for the algorithm of Sect. 2.6.1 nor our parameters listed in this section. In other words, our computations of images from experimental data were **unbiased.**

When solving equations (2.49) for functions $q_{n,i}$ (Sect. 2.6.1) in our computations, we have used in (2.49) $\overline{s}$-derivatives of tails $\partial_{\overline{s}} V_{n,i}(x, \overline{s})$ instead of tails $V_{n,i}(x, \overline{s})$ themselves. These derivatives were calculated via finite differences, similarly with (5.22). We remind that by (2.19) (Sect. 2.3) one should expect that

$$|\partial_{\overline{s}} V_{n,i}(x, \overline{s})|_{2+\alpha} << |V_{n,i}(x, \overline{s})|_{2+\alpha}. \tag{5.23}$$

Hence, the replacement of $V_{n,i}(x,\overline{s})$ with $\partial_{\overline{s}}V_{n,i}(x,\overline{s})$ goes along well with the first approximate mathematical model; see Sect. 2.8.4 for some details. At the same time, when computing functions $\varepsilon_r^{(n,i)}(x)$ via (5.24), we have used the function $V_{n,i}(x,\overline{s})$ itself rather than its derivative $\partial_{\overline{s}}V_{n,i}(x,\overline{s})$.

Suppose that we have computed the function $q_{n,i}(x)$. Then, we find the approximation $\varepsilon_r^n(x)$ for the function $\varepsilon_r(x)$ via backward calculation using (3.4) as

$$\varepsilon_r^{(n,i)}(x) = \begin{cases} f_{n,i}(x) := \Delta v_{n,i} + s_n^2 (\nabla v_{n,i})^2, x \in \Omega, \text{ if } f_{n,i}(x) \geq 1, \\ 1, \text{ if } f_{n,i}(x) < 1, \end{cases} \tag{5.24}$$

$$v_{n,i}(x) = -hq_{n,i}(x) - h\sum_{j=0}^{n-1} q_j(x) + V_{n,i}(x),$$

where $q_0 \equiv 0$ and $V_{n,i}(x)$ is the corresponding approximation for the tail function. We make the cut-off to unity in (5.24) because of (5.4).

The parameter of the CWF was $\lambda = 50$. Likewise, as it is quite often the case in imaging, we have made truncations to unity of those computed functions $\varepsilon_r^{(n,i)}(x)$ which were below a certain threshold. More precisely, for each $n$, we have chosen a cut-off value $C_{\text{cut}}(n) > 0$ and have assigned a new value $\tilde{\varepsilon}_r^{(n,i)}(x)$ for the function $\varepsilon_r^{(n,i)}(x)$ as

$$\tilde{\varepsilon}_r^{(n,i)}(x) = \begin{cases} \varepsilon_r^{(n,i)}(x), \text{ if } \varepsilon_r^{(n,i)}(x) > 1 + C_{\text{cut}}(n), \\ 1, \text{ if } \varepsilon_r^{(n,i)}(x) \in [1, 1 + C_{\text{cut}}(n)]. \end{cases} \tag{5.25}$$

Note that by (5.24), $\varepsilon_r^{(n,i)}(x) \geq 1$, $\forall x \in \Omega$. The numbers $C_{\text{cut}}(n)$ were chosen as follows:

$$C_{\text{cut}}(1) = 0, C_{\text{cut}}(2) = 0.2, C_{\text{cut}}(3) = C_{\text{cut}}(4) = 0.8, C_{\text{cut}}(5) = 0.6,$$
$$C_{\text{cut}}(6) = C_{\text{cut}}(7) = 0.4, C_{\text{cut}}(8) = 0.8.$$

We now define stopping rules of iterations for functions $q_{n,1}^k$ with respect to the nonlinear term as well as for functions $\{q_{n,i}\}$ with respect to the tails. These rules are almost the same as in Sect. 4.15.2. Consider the planar surface $P_{\tilde{h}}$ which is parallel to the surface $P$ in (5.9). The surface $P_{\tilde{h}}$ is obtained from the surface $P$ via shifting upward by $\tilde{h} = 0.2$:

$$P_{\tilde{h}} = \left\{(x,y,z) : (x,y) \in [-2.4, 2.4] \times [-1.4, -1.4], z = -2.4 + \tilde{h} = -2.2\right\}.$$

Let $\Omega' = \{(x,y) \in [-2.4, 2.4] \times [-1.4, -1.4]\}$ be the orthogonal projection of both surfaces $P$ and $P_{\tilde{h}}$ on the $(x,y)$ plane. Consider norms

$$F_n^k = ||q_{n,1}^k|_{P_{\tilde{h}}} - \overline{\psi}_n||_{L_2(\Omega')}.$$

We stop iterations of functions $q_{n,1}^k$ when either $F_n^{k+1} \geq F_n^k$ or $\left|F_n^k - F_n^{k-1}\right| \leq \varepsilon$, where $\varepsilon = 0.001$ is a small tolerance number of our choice. Next, we iterate with respect to the tails. We similarly introduce norms $F_{n,i} = ||q_{n,i}|_{P_{\tilde{h}}} - \overline{\psi}_n||_{L_2(\Omega')}$ and use the same stopping rule as the one for $F_n^k$.

We now describe the stopping rule for computing functions $\varepsilon_r^{(n)}(x)$. Let

$$a_n = \frac{\left\|\tilde{\varepsilon}_r^{(n)} - \tilde{\varepsilon}_r^{(n-1)}\right\|_{L_2(\Omega)}}{\left\|\tilde{\varepsilon}_r^{(n-1)}\right\|_{L_2(\Omega)}}, \; b_n = \frac{a_n}{a_{n-1}}.$$

### 5.7.1 *Stopping Rule for*

$\varepsilon_r^{(n)}$:

$$\text{If} \begin{cases} b_n \in [1.9, 4] \text{ and } n > 3, \text{ then take the final solution } \varepsilon_r^f = \varepsilon_r^{(n)}, \\ b_n > 4 \text{ and } n > 3, \text{ then take the final solution } \varepsilon_r^f = \varepsilon_r^{(n-1)}, \\ \text{alternatively compute } \varepsilon_r^{(n+1)}. \end{cases} \tag{5.26}$$

We have chosen $n > 3$ in (5.26) because we have observed in our work with computationally simulated data that images are becoming more or less close to the correct ones only starting from $n = 4$.

## 5.8 Reconstruction by the Approximately Globally Convergent Numerical Method

### 5.8.1 *Dielectric Inclusions and Their Positions*

Our dielectric inclusions to be imaged were two wooden cubes of 40 mm size of the side of the first cube and 60-mm size of the side of the second cube; see Table 5.1.

Let $CL$ be the center line, i.e., the straight line which is orthogonal to the plane $P$ and which passes through the source of EM waves. Then $CL = \{(x, y, z) : x = y = 0\}$. We have placed both those cubes in two positions. In the first position, the center of each cube was on $CL$. In the second position, the center was shifted off $CL$ by 10 mm in the positive direction of $x$ axis (0.2 in dimensionless units). In addition, we have used the third position for cube number 1. In the third position, the center of this cube was shifted by 60 mm off $CL$ in the positive direction of the $x$ axis (1.2 in dimensionless variables), which was rather far from $CL$. We have observed on the experimental data that since we had a spherical rather than a plane wave, then the magnitude of the EM field has significantly

**Table 5.1** Sizes and coordinates of centers of two wooden cubes used in experiments

| Cube number | Original sizes, mm | Dimensionless sizes | Dimensionless coordinates of centers |
|---|---|---|---|
| 1 | $40 \times 40 \times 40$ | $0.8 \times 0.8 \times 0.8$ | $(0, 0, -1.2)$ |
| 2 | $60 \times 60 \times 60$ | $1.2 \times 1.2 \times 1.2$ | $(0.2, 0, -1.2)$ |

Source: M.V. Klibanov, M.A. Fiddy, L. Beilina, N. Pantong and J. Schenk, Picosecond scale experimental verification of a globally convergent numerical method for a coefficient inverse problem, *Inverse Problems*, 26, 045003, doi:10.1088/0266-5611/26/4/045003, 2010. © IOP Publishing. Reprinted with permission

**Table 5.2** Positions of centers of two wooden cubes to be imaged in six cases. The difference between cases 1.1(1) and 1.1(2) is that they were measured on two different days for the same position of cube 1

| Cube number | Case number | Center |
|---|---|---|
| 1 | 1.1(1) | $(0, 0, -1.2)$ |
| 1 | 1.1(2) | $(0, 0, -1.2)$ |
| 1 | 1.2 | $(0.2, 0, -1.2)$ |
| 1 | 1.3 | $(1.2, 0, -1.2)$ |
| 2 | 2.1 | $(0, 0, -1.2)$ |
| 2 | 2.2 | $(0.2, 0, -1.2)$ |

Source: M.V. Klibanov, M.A. Fiddy, L. Beilina, N. Pantong and J. Schenk, Picosecond scale experimental verification of a globally convergent numerical method for a coefficient inverse problem, *Inverse Problems*, 26, 045003, doi:10.1088/0266-5611/26/4/045003, 2010. © IOP Publishing. Reprinted with permission

decayed when the point has moved rather far from $CL$. So the goal of placing cube number 1 in the third position was to see how this decay of the magnitude of the EM field would affect the image quality. Due to some logistical reasons, we have measured the scattering field from cube number 1 in the first position twice: in two consecutive days. Therefore, we have obtained total six (6) pieces of data for the case when either of those two cubes was present. In addition, the data for the reference medium, was measured only once. Table 5.2 lists all six cases.

### 5.8.2 Tables and Images

We have made computations using the approximately globally convergent algorithm of Sect. 2.6.1. Functions $\psi_n(x)$ in (5.22) were used as boundary conditions. The stopping rules were the same as the one in Sect. 5.7. We point out again that we did not know in advance values refractive indices of above wooden cubes. Therefore, we were **unbiased** when applying stopping rules. Table 5.3 presents numbers $a_n$ and $b_n = a_n/a_{n-1}$ for the case 1.1(1) (see Table 5.2 for labeling of our cases). It is clear from the stopping rule (5.26) why we have stopped in this table at $n = 6$.

**Table 5.3** Computational results for the case 1.1(1); see Table 5.2 for labeling of cases and (49) for the stopping rule

| Iter., $n$ | $\varepsilon_r^{(n)}$ | $a_n$ | $b_n$ | $\varepsilon_r^f$ | $n_f = \sqrt{\varepsilon_r^f}$ |
|---|---|---|---|---|---|
| 2 | 1.28 | 0.027 | 0.21 | | |
| 3 | 2.53 | 0.209 | 7.74 | | |
| 4 | 2.9 | 0.160 | 0.76 | | |
| 5 | 3.76 | 0.266 | 1.66 | | |
| 6 | 4.66 | 0.580 | 2.18 | $\varepsilon_r^f = \varepsilon_r^{(6)} = 4.66$ | 2.16 |
| 7 | 5.6 | 0.683 | 1.18 | | |
| 8 | 8.1 | 0.809 | 1.18 | | |

Source: M.V. Klibanov, M.A. Fiddy, L. Beilina, N. Pantong and J. Schenk, Picosecond scale experimental verification of a globally convergent numerical method for a coefficient inverse problem, *Inverse Problems*, 26, 045003, doi:10.1088/0266-5611/26/4/045003, 2010. © IOP Publishing. Reprinted with permission

**Table 5.4** Computational results for five cases; see (5.8.2) for the stopping rule and Table 5.2 for labeling of cases. The rest of iterations for all these five cases was similar with Table 5.3. Comparison of this table with (5.26) makes it clear why either of function $\varepsilon_r^{(n)}$ or $\varepsilon_r^{(n-1)}$ was chosen as the final imaging result $\varepsilon_r^f$

| Case | Iter., $n$ | $b_n$ | $\varepsilon_r^f$ | $n_f = \sqrt{\varepsilon_r^f}$ |
|---|---|---|---|---|
| 1.1(2) | 5 | 2.07 | $\varepsilon_r^f := \varepsilon_r^{(5)} = 4$ | 2 |
| 1.2 | 6 | 2.40 | $\varepsilon_r^f := \varepsilon_r^{(6)} = 4.65$ | 2.16 |
| 1.3 | 6 | 3.57 | $\varepsilon_r^f := \varepsilon_r^{(6)} = 4.82$ | 2.19 |
| 2.1 | 6 | 5.74 | $\varepsilon_r^f := \varepsilon_r^{(5)} = 2.98$ | 1.73 |
| 2.2 | 6 | 5.36 | $\varepsilon_r^f := \varepsilon_r^{(5)} = 3.19$ | 1.79 |

Source: M.V. Klibanov, M.A. Fiddy, L. Beilina, N. Pantong and J. Schenk, Picosecond scale experimental verification of a globally convergent numerical method for a coefficient inverse problem, *Inverse Problems*, 26, 045003, doi:10.1088/0266-5611/26/4/045003, 2010. © IOP Publishing. Reprinted with permission

Behavior of numbers $a_n$ and $b_n$ for other cases was similar. Table 5.4 presents only numbers $b_n$ for the final iteration. Again, the stopping rule (5.26) explains the choice of the final image $\varepsilon_r^f$. Figures 5.5 and 5.6 display computed images. Figure 5.5 is for the case 1(1). One can see from Fig. 5.5g, h how the image "explodes" after the stopping criterion (5.26) is reached at $n = 6$; see Table 5.3. Figure 5.6 show that locations of inclusions are imaged with a good accuracy. The latter is true even in the most difficult case 1.3 when the inclusion was located far off the center line $CL$, which meant a low amplitude of the signal; see Sect. 5.8.1.

Still, shapes of abnormalities are not imaged well on Fig. 5.6. Recall, however, that our goal for the first stage of our two-stage numerical procedure was twofold: (1) to obtain accurate locations of inclusions and (2) to accurately image refractive indexes in them. However, we did not have the goal to accurately image shapes of inclusions on the first stage of our two-stage numerical procedure.

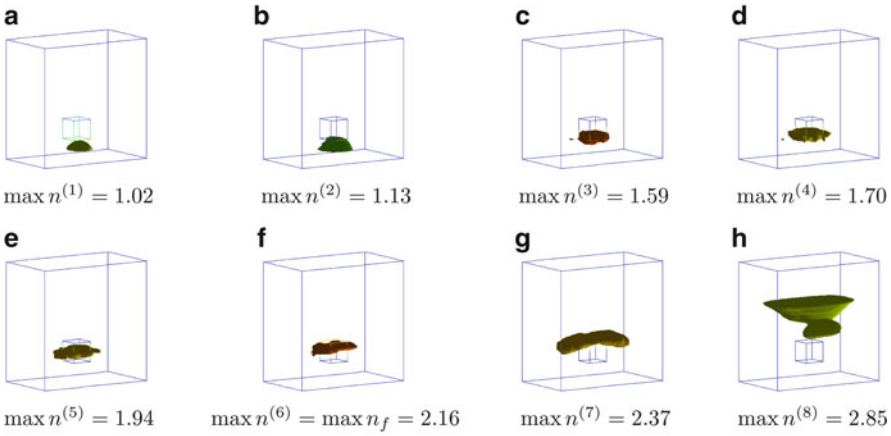


**Fig. 5.5** (**a**)–(**h**) represent the dynamics of the sequence of images for the case number 1.1(1). Maximal values of refractive indexes $\max_{\overline{P}} n^{(k)} = \sqrt{\max_{\overline{P}} \varepsilon_r^{(k)}}$ are displayed. Each image represents the level surface $x : n^{(k)}(x) = \max_{\overline{P}} n^{(k)}(x)$. The final image is presented on (**f**). (**h**) shows that the image "explodes" on the second iteration after the stop; see the stopping rule (5.26) and Table 5.3. Source: M. V. Klibanov, M. A. Fiddy, L. Beilina, N. Pantong and J. Schenk, Picosecond scale experimental verification of a globally convergent numerical method for a coefficient inverse problem, *Inverse Problems*, 26, 045003, doi:10.1088/0266-5611/26/4/045003, 2010. © IOP Publishing. Reprinted with permission

### *5.8.3 Accuracy of the Blind Imaging*

We have independently measured refractive indices **after** the above images were obtained. Those measurements were performed by two methods which are well established in Physics: the waveguide method [133] and the oscilloscope method [71]. In the case of the waveguide Method the measurement error was 11% for cube number 1 and 3.5% for cube number 2. In the case of the oscilloscope method the measurement error was 6% for both cubes. Tables 5.5 and 5.6 display both errors: in computations and direct measurements. Only maximal values of computed refractive indices are presented in these tables. One can see that the computational error does not exceed the measurement error in five (5) out of six (6) cases. And it exceeds the measurement error in the sixth case by less than 2%.

Therefore, we conclude that the approximately globally convergent numerical method has produced images of an excellent accuracy for both locations and refractive indices of dielectric abnormalities in blind testing. Furthermore, this result was obtained for the case of a huge misfit between the experimental and computationally simulated data. Therefore, this accuracy fully justifies our data pre-processing procedure.

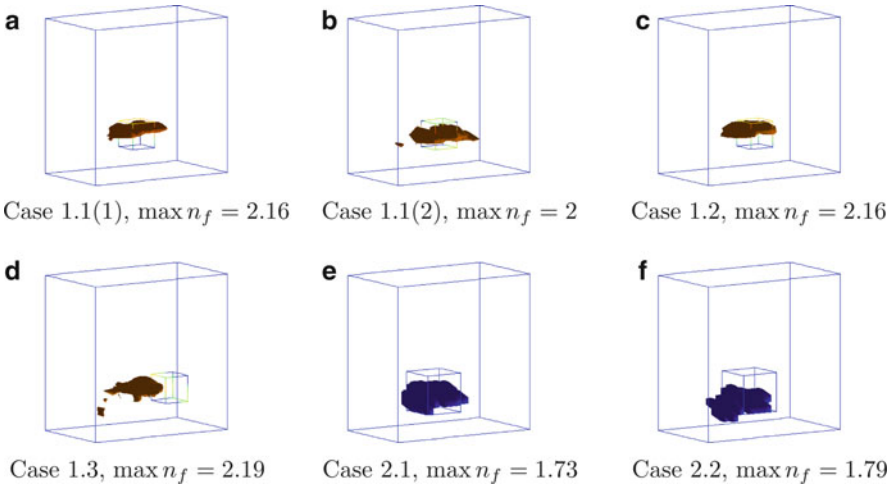


**Fig. 5.6** Resulting images. It should be kept in mind that we did not have a goal to image shapes of inclusions accurately. Rather, our goal was only to image their locations and maximal values of refractive indexes $n_f(x) = \sqrt{\varepsilon_r^f}$. On each figure, $n_f(x) = \max n_f$ for all points of the image of the corresponding cube. In addition to the cut-offs (5.25), we have made the last postprocessing cut-off of the imaged function $\varepsilon_r^f$ each figure just to make it look better. That cut-off was made around the center of the image. For all cases, the dynamics of the change of images of functions $\varepsilon_r^{(n)}$ with iterations was similar with one on Fig. 5.5a–h. Source: M. V. Klibanov, M. A. Fiddy, L. Beilina, N. Pantong and J. Schenk, Picosecond scale experimental verification of a globally convergent numerical method for a coefficient inverse problem, *Inverse Problems*, 26, 045003, doi:10.1088/0266-5611/26/4/045003, 2010. © IOP Publishing. Reprinted with permission

**Table 5.5** Comparison of imaging results of values of refractive indexes for six cases of Table 5.2 with measurements by the waveguide method

| Case | Blindly imaged $n := n_f$ | Measured $n$, error (%) | Imaging error (%) |
|---|---|---|---|
| 1.1(1) | 2.16 | 2.07, 11 | 4.3 |
| 1.1(2) | 2 | 2.07, 11 | 3.4 |
| 1.2 | 2.16 | 2.07, 11 | 4.3 |
| 1.3 | 2.19 | 2.07, 11 | 5.8 |
| 2.1 | 1.73 | 1.71, 3.5 | 1.2 |
| 2.2 | 1.79 | 1.71, 3.5 | 4.7 |

Source: M.V. Klibanov, M.A. Fiddy, L. Beilina, N. Pantong and J. Schenk, Picosecond scale experimental verification of a globally convergent numerical method for a coefficient inverse problem, *Inverse Problems*, 26, 045003, doi:10.1088/0266-5611/26/4/045003, 2010. © IOP Publishing. Reprinted with permission

**Table 5.6** Comparison of imaging results of values of refractive indexes for six cases of Table 5.2 with measurements by the oscilloscope method

| Case | Blindly imaged $n := n_f$ | Measured $n$, error (%) | Imaging error (%) |
|---|---|---|---|
| 1.1(1) | 2.16 | 2.17, 6 | 0.5 |
| 1.1(2) | 2 | 2.17, 6 | 7.8 |
| 1.2 | 2.16 | 2.17, 6 | 0.5 |
| 1.3 | 2.19 | 2.17, 6 | 1 |
| 2.1 | 1.73 | 1.78, 6 | 2.8 |
| 2.2 | 1.79 | 1.78, 6 | 0.56 |

Source: M.V. Klibanov, M.A. Fiddy, L. Beilina, N. Pantong and J. Schenk, Picosecond scale experimental verification of a globally convergent numerical method for a coefficient inverse problem, *Inverse Problems*, 26, 045003, doi:10.1088/0266-5611/26/4/045003, 2010. 

### 5.8.4 *Performance of a Modified Gradient Method*

We have decided to compare performances of the approximately globally convergent numerical method with a modified gradient method for the case of above experimental data. Since the gradient method is outside of our main focus, our discussion is intentionally brief here. First, we need to introduce the Tikhonov functional for the above CIP in the pseudo frequency domain and derive its Fréchet derivative. We call the technique of this section the "modified gradient method" because instead of making usual steps in the gradient method, we find the zero of the Fréchet derivative of the Tikhonov functional via solving an equation with a contractual mapping operator. Our derivation of the Fréchet derivative of the Tikhonov functional is similar with the heuristic derivation in Sect. 4.4.

Let $u(x,t)$ be the solution of the problem (5.1), (5.2) and

$$w(x,s) = \int_0^\infty u(x,t)\, e^{-st} dt. \tag{5.27}$$

Then by Theorem 2.7.2,

$$\Delta w - s^2 \varepsilon_r(x)\, w = -\delta(x - x_0), \tag{5.28}$$

$$\lim_{|x|\to\infty} w(x,s) = 0. \tag{5.29}$$

Let $\tilde{g}(x,s)$ be the Laplace transform (5.27) of the function $g(x,t)$ in (5.6). Then

$$w(x,s)\,|_{\partial\Omega} = \tilde{g}(x,s). \tag{5.30}$$

Since by (5.3), the coefficient $\varepsilon_r(x) = 1$ outside of $\Omega$, then we can uniquely solve the boundary value problem (5.28), (5.29), (5.30) in the domain $\mathbb{R}^3 \setminus \Omega$ for every value of $s$ of our interest. Hence, we can uniquely find the normal derivative

$p(x,s) = \partial_n w(x,s)\,|_{\partial\Omega}$. Hence, we obtain the so-called "state" boundary value problem for the function $w$ inside the domain $\Omega$:

$$\begin{aligned} \Delta w - s^2 \varepsilon_r(x)\, w &= 0 \text{ in } \Omega, \\ \partial_n w(x,s)\,|_{\partial\Omega} &= p(x,s). \end{aligned} \tag{5.31}$$

In addition, consider the so-called "adjoint" boundary value problem for the function $\lambda$:

$$\begin{aligned} \Delta\lambda - s^2 \varepsilon_r(x)\,\lambda &= 0 \text{ in } \Omega, \\ \partial_n \lambda(x,s)\,|_{\partial\Omega} &= (w\,|_{\partial\Omega} - \tilde{g})(x,s). \end{aligned} \tag{5.32}$$

The idea of the gradient method is to find a zero of the Fréchet derivative of the Tikhonov functional:

$$E(\varepsilon_r) = \frac{1}{2}\int\limits_{s_1}^{s_2}\int\limits_{\partial\Omega} (w\,|_{\partial\Omega} - \tilde{g})^2\, d\sigma_x ds + \frac{\alpha}{2}\int\limits_{\Omega}\left(\varepsilon_r(x) - \varepsilon_r^{(0)}(x)\right)^2 dx,$$

where $(s_1, s_2)$ is an interval of pseudo frequencies, $w = w(x,s;\varepsilon_r)$ is the solution of the problem (5.31), and $\varepsilon_r^{(0)}$ is a first approximation for the unknown coefficient $\varepsilon_r$: In order to simplify the derivation of the Fréchet derivative of this functional, consider the associated Lagrangian $L(\varepsilon_r)$,

$$L(\varepsilon_r) = E(\varepsilon_r) + \int\limits_{s_1}^{s_2}\int\limits_{\partial\Omega} p\lambda\, d\sigma_x ds - \int\limits_{s_1}^{s_2}\int\limits_{\Omega}\left(\nabla w \nabla\lambda + s^2\varepsilon_r(x) w\lambda\right) dx ds. \tag{5.33}$$

It follows from the definition of the weak solution of the problem (5.31) that the integral term in (5.33) equals zero. Hence, $L(\varepsilon_r) = E(\varepsilon_r)$ for all admissible function $\varepsilon_r(x)$. To figure out the Fréchet derivative $L'(\varepsilon_r)$, we need to vary in (5.33) the function $\varepsilon_r$ via considering the function $\varepsilon_r(x) + b(x)$, where the functions $b(x)$ is an appropriate small perturbation of the function $\varepsilon_r(x)$. But since functions $w = w(x,s;\varepsilon_r)$ and $\lambda = \lambda(x,s;\varepsilon_r)$ depend on $\varepsilon_r$ as solutions of boundary value problems (5.31) and (5.32), then we should also consider respective variations of these functions. In other words, we should consider Fréchet derivatives of functions $w(x,s;\varepsilon_r)$, $\lambda(x,s;\varepsilon_r)$ with respect to $\varepsilon_r$. These Fréchet derivatives are actually solutions of such boundary value problems, which are obtained via the linearization of problems (5.31) and (5.32) with respect to $b$. Finally, the linear, with respect to $b(x)$, part of the difference $L(\varepsilon_r + b) - L(\varepsilon_r)$ is $L'(\varepsilon_r)(b)$. Again, the necessary formalism for the hyperbolic case can be found in Chap. 4, and our elliptic case is similar. So, finally, we obtain

$$E'(\varepsilon_r) = \alpha\left(\varepsilon_r - \varepsilon_r^{(0)}\right)(x) - \int\limits_{s_1}^{s_2} s^2 (w\lambda)(x,s;\varepsilon_r)\, ds.$$

At a point of a minimum of the functional $E(\varepsilon_r)$ one should have $E'(\varepsilon_r) = 0$. Therefore, we should solve the following equation:

$$\varepsilon_r(x) = \frac{1}{\alpha}\int_{s_1}^{s_2} s^2 (w\lambda)(x,s;\varepsilon_r)\,ds + \varepsilon_r^{(0)}(x), x \in \Omega. \tag{5.34}$$

It can be proven that one can choose the number $\zeta = (s_2 - s_1)/\alpha$ so small that equation (5.34) becomes an equation with the contraction mapping operator, which, therefore, can be solved iteratively. Of course, the number $\zeta$ should not be too small since, otherwise, the resulting solution would be too close to the initial guess $\varepsilon_r^{(0)}$. So, one should choose optimal parameters $s_1, s_2, \alpha$.

Temporary denote $\mathbf{x} = (x, y, z)$. When applying the modified gradient method (5.34) to the experimental data, our starting point for iterations was $\varepsilon_r^{(0)} \equiv 1$. In other words, since any gradient-like method is a locally convergent one, we have assumed that we know the background medium in the domain $\Omega$. This is unlike the approximately globally convergent method. We have observed that the function $\lambda\left(\mathbf{x}, s; \varepsilon_r^{(0)}\right) = \lambda(\mathbf{x}, s; 1) < 0$. At the same time, by Theorem 2.7.2, $w\left(\mathbf{x}, s; \varepsilon_r^{(0)}\right) = w(\mathbf{x}, s; 1) > 0$, and we have also observed this inequality computationally. Hence, it follows from (5.34) that $\varepsilon_r^{(1)} < 1$, where $\varepsilon_r^{(1)}$ is the result of the first iteration of the solution of the problem (5.34) with the contraction mapping operator. We have tried a variety of numbers $s_1, s_2, \alpha$ in (5.34), some of which have ensured the contraction mapping property. Still, with all these parameters, we have obtained functions $\varepsilon_r^{(n)} < 1$ for all iteration numbers $n$. However, by (5.4), we should have $\varepsilon_r(x) \geq 1$.

We have a close to rigorous explanation of the negative values of the function $\lambda(\mathbf{x}, s; 1)$. Consider, for example, the case when the domain $\Omega$ is the half space, $\Omega = \{z > -2.4\}$ (see (5.8)). Changing variables $z' := z + 2.4$ and leaving the same notation for the new variable as for the old one (for brevity), we obtain $\Omega = \{z > 0\}$. In addition, assume that the condition $\lim_{|x|\to\infty} \lambda(\mathbf{x}, s; 1) = 0$ is imposed and also that $\lim_{|\mathbf{x}|\to\infty} (w|_{z=0} - \tilde{g}) = 0$. Consider the function $Q(\mathbf{x}, \boldsymbol{\xi})$:

$$Q(\mathbf{x}, \boldsymbol{\xi}) = \frac{\exp(-s|\mathbf{x} - \boldsymbol{\xi}|)}{4\pi|\mathbf{x} - \boldsymbol{\xi}|} + \frac{\exp\left(-s\left|\mathbf{x} - \boldsymbol{\xi}'\right|\right)}{4\pi\left|\mathbf{x} - \boldsymbol{\xi}'\right|}, \boldsymbol{\xi}' = (\xi_1, \xi_2, -\xi_3).$$

It can be easily verified that $Q(\mathbf{x}, \boldsymbol{\xi})$ is the Green's function with the Neumann boundary condition in the half space $\{z > 0\}$ for the operator $\Delta - s^2$. Hence, by (5.31),

$$\lambda(\mathbf{x}, s, 1) = \int_{\mathbb{R}^2} Q(\mathbf{x}, \xi_1, \xi_2, 0)\left[w((\xi_1, \xi_2, 0), s; 1) - \tilde{g}(\xi_1, \xi_2, s)\right] d\xi_1 d\xi_2.$$

We have observed computationally that $w((\xi_1, \xi_2, 0), s; 1) - \tilde{g}(\xi_1, \xi_2, s) \leq 0$ for all reasonable values of $\xi_1, \xi_2, s$. Hence, $\lambda(\mathbf{x}, s; 1) \leq 0$.

In addition, we have observed computationally that for all reasonable values of the pseudo frequency $s$ maximal absolute values of functions $w$ and $\lambda$ were too small. So that

$$\max_{x \in \overline{\Omega}} \left[ s^2 \left| w\lambda \right| (x, s) \right] \leq 3 \cdot 10^{-4}.$$

By (5.34), this means, however, that in order for the function $\varepsilon_r$ to be rather significantly different from $\varepsilon_r^{(0)} \equiv 1$, i.e., in order to obtain above inclusion/background contrasts, one should choose a very small regularization parameter $\alpha$. For example, to get $\varepsilon_r^f = 4.66$ within the imaged inclusion (Table 5.3), one should have $\alpha \approx 8 \cdot 10^{-5}$. It is well known, however, that exceedingly small values of regularization parameters affect results quite negatively.

We, therefore conclude that the modified gradient method (5.34) is inapplicable here. However, since any version of the gradient method should still use the gradient $E'(\varepsilon_r)$, then it is unlikely that other versions of the gradient method are applicable here. This likely means that locally convergent numerical methods are inapplicable in the pseudo frequency domain. Thus, it seems to be that our approximately globally convergent technique is the *single* choice for this kind of experimental data.

## 5.9 Performance of the Two-Stage Numerical Procedure

We show in this section how the two-stage numerical procedure works for the above experimental data. Recall that the first stage has provided us with accurate images of two components of dielectric abnormalities: locations and refractive indices; see Figure 5.6 as well as Tables 5.4 and 5.5. We now want to add the third component: the shape.

### *5.9.1 The First Stage*

We have recomputed images for two cases using the algorithm of the first stage. More precisely, those were cases which are listed on Table 5.2 as 5.1(1) and 5.2. For the convenience of the reader, we list these two cases in Table 5.7 again. Since parameters in computations for these two cases were a little bit different from those used in Sect. 5.8, our images were a little bit different also, although we have used the same stopping rule (5.26) as in Sect. 5.8. Figures 5.7 and 5.8 show how images were changing with iterations, which is similar with Figs. 5.5, 5.7c and 5.8c display final images for two cases of Table 5.7. Table 5.8 shows reconstructed refractive indices for these two cases as well as their comparisons with results of direct measurements by the wave guide method. One can again observe an excellent accuracy of the reconstruction of refractive indices.

**Table 5.7** Cases considered in the two-stage numerical procedure

| Cube number | Case number | Center |
|---|---|---|
| 1 | 1.1(1) | (0,0,−1.2) |
| 2 | 2.2 | (0.2,0,−1.2) |

Source: L. Beilina and M.V. Klibanov, Reconstruction of dielectrics from experimental data via a hybrid globally convergent/adaptive inverse algorithm, *Inverse Problems*, 26, 125009, doi:10.1088/0266-5611/26/12/125009, 2010. 

### 5.9.2 The Third Stage of Data Immersing

It is evident from Fig. 5.4a that the function $u_{\text{incl}}(x_m, t)$ is very noisy with respect to the positions of the detector $x_m \in P$. While the second stage of data immersing has worked in the "Laplace transform domain" (Sect. 5.6.2), we apply the adaptivity in the time domain. Hence, we now need to smooth somehow the function $u_{\text{incl}}(x_m, t)$. Although this smoothing can be done similarly with Sect. 5.6.2, this would not address the problem we face now. Indeed, it follows from (5.13) to (5.16) that we need to somehow obtain the proper data for the function $u(x,t)$ for $(x,t) \in P_{\text{obs}} \times (0,T)$ while having the data $u_{\text{incl}}(x_m, t)$ only for $x_m \in P$, where the rectangle $P$ is narrower than the rectangle:

$$P_{\text{obs}} = \{(x,y,z) : (x,y) \in (-3,3) \times (-2,2), z = -2.4\}.$$

This extension from $P$ in $P_{\text{obs}}$ is the subject of our third stage of data immersing.

Let $\varepsilon_r^{\text{glob}}(x)$ be the solution obtained on the first stage. Let $U(x,t)$ be the solution of the problem (5.11) for the case $\varepsilon_r(x) := \varepsilon_r^{\text{glob}}(x)$. Let $u_{\text{incl}}(x,t)$, $(x,t) \in P \times (0,T)$ be the standard linear interpolation of the discrete function $u_{\text{incl}}(x_m, t)$. Our third stage of data immersing consists in defining the function $u_{\text{immers}}(x,t)$ for $(x,t) \in P_{\text{obs}} \times (0,T)$ as

$$u_{\text{immers}}(x,t) = \begin{cases} u_{\text{incl}}(x,t), \text{ if } x \in P \text{ and } u_{\text{incl}}(x,t) \geq \beta \max_{\overline{P}} u_{\text{incl}}(x,t), \\ U(x,t), \text{ otherwise.} \end{cases} \tag{5.35}$$

The parameter $\beta \in (0,1)$ in (5.35) should be chosen in numerical experiments. In particular, it follows from (5.35) that

$$u_{\text{immers}}(x,t) = U(x,t) \text{ for } x \in P_{\text{obs}} \setminus P. \tag{5.36}$$

Taking into account (5.13), we set in (5.15) and (5.16)

$$g(x,t) := u_{\text{immers}}(x,t) \text{ for } (x,t) \in S'_T = P_{\text{obs}} \times (0,T). \tag{5.37}$$

Comparison of Fig. 5.9a, c, e with Fig. 5.9b, d, f shows that the third stage of data immersing not only allows to extend the data from $P$ to $P_{\text{obs}}$ but also significantly

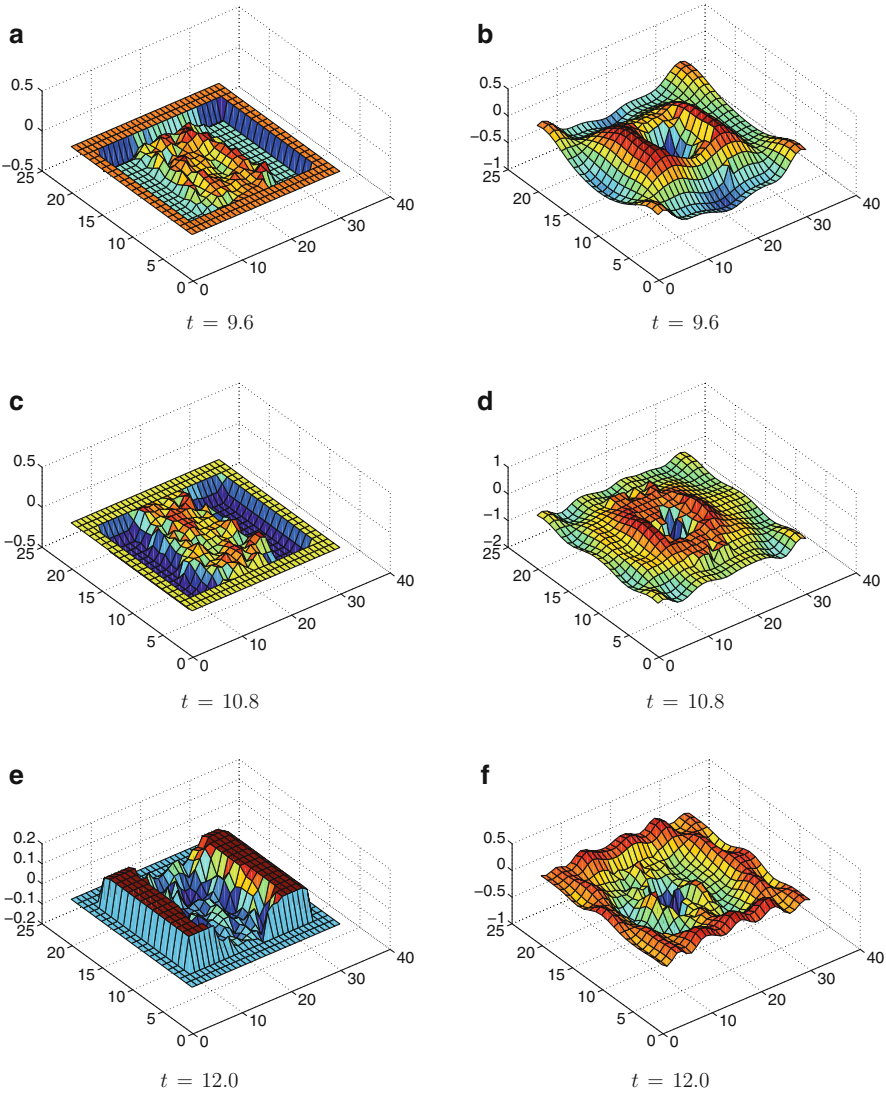


**Fig. 5.7** (**a**),(**c**),(**e**) The function $g(x,t), x \in P$ for cube No.1 (Table 5.1). This is the function $u_{\text{incl}}(x,t), x \in P$. However, to solve the adjoint problem (5.15) in the adaptivity, we need to know this function at a wider rectangle $x \in P_{\text{obs}}$; see Sect. 5.6. So, since $P \subset\subset P_{\text{obs}}$, we need to extend somehow the function $g(x,t)$ from $P$ to $P_{\text{obs}}$. This extension is carried out via the third stage of our data immersing procedure; see Sect. 5.6. (**b**),(**d**),(**f**) present the resulting immersed data with $\beta = 0.1$. Source: L. Beilina and M.V. Klibanov, Reconstruction of dielectrics from experimental data via a hybrid globally convergent/adaptive inverse algorithm, *Inverse Problems*, 26, 125009, doi:10.1088/0266-5611/26/12/125009, 2010. © IOP Publishing. Reprinted with permission

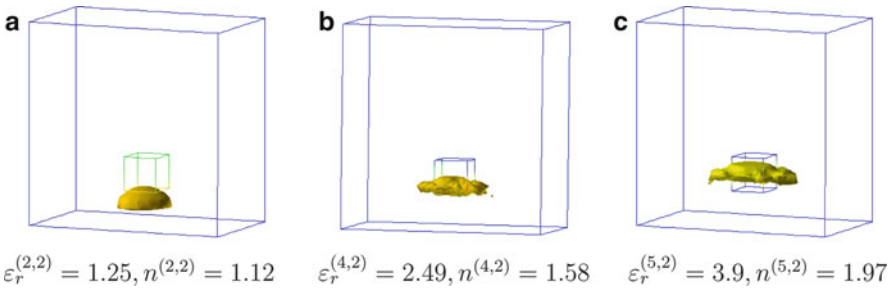


**Fig. 5.8** Spatial distributions of iteratively computed dielectric constants $\varepsilon_r^{(n,k)}$ and refractive indexes $n^{(n,k)} = \sqrt{\varepsilon_r^{(n,k)}}$ for the cube number 1 (Table 5.7). The final image corresponds to $n^{(5,2)} := n_{\text{glob}} = 1.97$. See Table 5.8 for the reconstruction accuracy. Recall that refractive indices rather than dielectric constants are actually measured experimentally. Source: L. Beilina and M.V. Klibanov, Reconstruction of dielectrics from experimental data via a hybrid globally convergent/adaptive inverse algorithm, *Inverse Problems*, 26, 125009, doi:10.1088/0266-5611/26/12/125009, 2010. © IOP Publishing. Reprinted with permission

**Table 5.8** Computed refractive indices on the first stage of the two-stage numerical procedure (second column). The third and fourth column show directly measured indices by the wave guide method and computational errors respectively

| Cube Number | Computed $n$ | Measured $n$, error (%) | Imaging error (%) |
|---|---|---|---|
| 1 | 1.97 | 2.17, 11 | 9.2 |
| 2 | 1.79 | 1.78, 3.5 | 0.5 |

Source: L. Beilina and M.V. Klibanov, Reconstruction of dielectrics from experimental data via a hybrid globally convergent/adaptive inverse algorithm, *Inverse Problems*, 26, 125009, doi:10.1088/0266-5611/26/12/125009, 2010. © IOP Publishing. Reprinted with permission

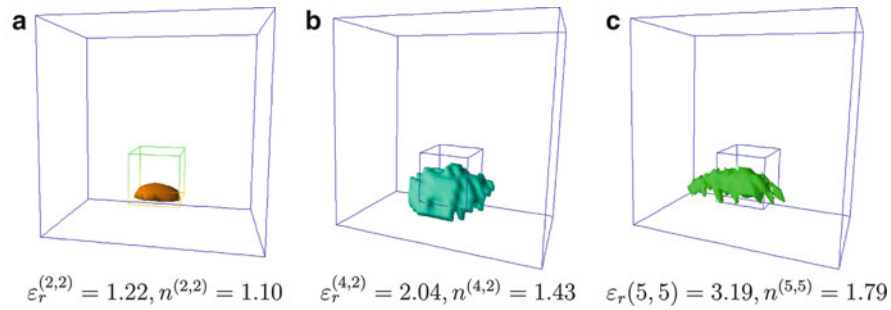


**Fig. 5.9** Spatial distributions of iteratively computed dielectric constants $\varepsilon_r^{(n,k)}$ and refractive indexes $n^{(n,k)} = \sqrt{\varepsilon_r^{(n,k)}}$ for the cube number 2 (Table 5.7). The final image corresponds to $n^{(5,5)} := n_{\text{glob}} = 1.79$, which is only 3.5% error compared with the experiment; see Table 5.8. Recall that refractive indices rather than dielectric constants are actually measured experimentally. Source: L. Beilina and M.V. Klibanov, Reconstruction of dielectrics from experimental data via a hybrid globally convergent/adaptive inverse algorithm, *Inverse Problems*, 26, 125009, doi:10.1088/0266-5611/26/12/125009, 2010. © IOP Publishing. Reprinted with permission

decreases the noise in the data compared with the function $u_{\text{incl}}(x,t)$ which was the result of the first immersing stage. Another important point here is that variations of the parameter $\beta$ in a wide range $\beta \in (0.1, 0.985)$ do not significantly affect results; see Fig. 5.15.

### 5.9.3 Some Details of the Numerical Implementation of the Adaptivity

The adaptivity in this case consists of two stages of mesh refinement:

**Stage 1.** On this stage, we use both first and second mesh refinement recommendations (5.17) and (5.18) of Sect. 5.5. In doing so, we use the same parameters $\beta_1, \beta_2, \alpha$ as ones in (5.19).

**Stage 2.** On this stage, we use only the second mesh refinement recommendation (5.18) with parameters $\beta_2, \alpha$ listed in (5.19).

Just as in Sect. 4.16.2, we use a cut-off parameter $B_{\text{cut}}$. In other words, we set

$$\varepsilon_{r,h}(x) = \begin{cases} \varepsilon_{r,h}(x), \text{ if } |\varepsilon_{r,h}(x) - \varepsilon_r^{\text{glob}}(x)| \geq B_{\text{cut}}, \\ \varepsilon_r^{\text{glob}}(x), \text{ elsewhere.} \end{cases} \tag{5.38}$$

Specific values of the parameter $B_{\text{cut}}$ are given below.

In addition, we impose the upper bound $d$ on functions $\varepsilon_{r,h}(x)$; see (5.4). In other words, we enforce that

$$\varepsilon_{r,h}(x) \in C_M = \{1 \leq \varepsilon_{r,h}(x) \leq d\}.$$

We find good estimates for the number $d$ from results of the first stage since approximate global convergence Theorems 2.8.2 and 2.9.4 guarantee that the function $\varepsilon_r^{\text{glob}}(x)$ is close to the correct solution. Concrete values of $d$ are given below.

### 5.9.4 Reconstruction Results for Cube Number 1

We have used the function $\varepsilon_r^{\text{glob}}(x)$ as the starting point for iterations; see Fig. 5.7c for the image of this function. Also, in addition to (5.17), we took the following values of parameters $d$ in (5.4), $\beta$ in (5.35) and $B_{\text{cut}}$ in (5.38):

$$d = 4.4, \ \beta = 0.985, \ B_{\text{cut}} = 2.$$

We have chosen $d = 4.4$ since by Table 5.8, $\max \varepsilon_r^{\text{glob}}(x) = (1.97)^2 \approx 3.9$. Hence, the admissible set of parameters in this case is

$$\varepsilon_r(x) \in C_M = \{1 \leq \varepsilon_r(x) \leq 4\}.$$

As to the parameters $\alpha, \beta_1, \beta_2$, see (5.19).

#### 5.9.4.1 The First Stage of Mesh Refinements

First, using the same coarse mesh as the one on the first stage, we have not observed any image improvement, which is similar with numerical results of Sects. 4.15.3 and 4.16.2. To figure out when we should stop mesh refinements, we proceed similarly with Sects. 4.15.3 and 4.16.2. Namely, we analyze norms

$$\|g - u\|_{L_2(S'_T)} = \|u_{\text{immers}} - u\|_{L_2(S'_T)}; \tag{5.39}$$

see (5.37). These norms decrease with the number of mesh refinements up to the third mesh refinement. Next, on the fourth mesh refinement, the norm (5.39) slightly increases. Hence, similarly with Sects. 4.15.3 and 4.16.2, relaxation Theorems 4.9.3 and 4.11.4 tell us that the third mesh refinement should be the final one.

The resulting image is displayed on Fig. 5.10. Comparison of Figs. 5.10 and 5.7c shows that the adaptivity has improved the image of the shape. Also, refractive indices on both figures are the same. However, the shape of the abnormality is not yet imaged well.

#### 5.9.4.2 The Second Stage of Mesh Refinements

Let $\overline{\varepsilon}_r(x)$ be the coefficient reconstructed on the first stage of mesh refinements. The image of $\overline{\varepsilon}_r(x)$ is depicted on Fig. 5.10. Analyzing the image of Fig. 5.10 computationally, we have observed that the imaged inclusion of this figure is contained in the subdomain $\tilde{\Omega} \subset \Omega$, where

$$\tilde{\Omega} = \{(x, y, z) \in [-0.5, 0.5] \times [-0.6, 0.6] \times [-1.4, -0.5]\}.$$

On this stage of mesh refinements, we use only the second mesh refinement recommendation and refine the mesh in neighborhoods of all such points $x$ that

$$x \in \left\{\overline{\varepsilon}_r(x) \geq 0.2 \max_{\overline{\Omega}} \overline{\varepsilon}_r(x)\right\} \cap \tilde{\Omega}.$$

The same stopping criterion as the one in Sects. 4.15.3 and 4.16.2 was used again. Recall that relaxation Theorems 4.9.3 and 4.11.4 help in this case.

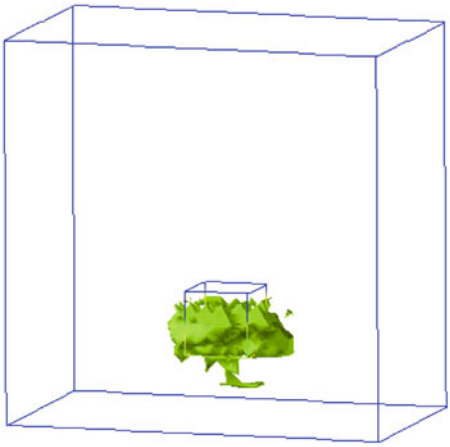


**Fig. 5.10** The reconstruction result for the first stage of the adaptivity for the cube number 1. Maximal values of the imaged coefficient are shown for the third refined mesh. The shape is not yet well reconstructed, although a comparison with Fig. 5.8c shows an improvement. The refractive index is reconstructed accurately (Table 5.8). Source: L. Beilina and M.V. Klibanov, Reconstruction of dielectrics from experimental data via a hybrid globally convergent/adaptive inverse algorithm, *Inverse Problems*, 26, 125009, doi:10.1088/0266-5611/26/12/125009, 2010. © IOP Publishing. Reprinted with permission

Figure 5.12 displays the final image. Comparison of this figure with Fig. 5.10 shows an improvement of the image of the shape of the cube Number 1. Refractive indices are the same in both cases and are equal to the one computed by the approximately globally convergent algorithm.

### 5.9.5 *Reconstruction Results for the Cube Number 2*

Just as above, we took the function $\varepsilon_r^{glob}(x)$ as the starting point for iterations. The image of this function is displayed on on Fig. 5.8c. See (5.19) for parameters $\alpha, \beta_1, \beta_2$. Since by the second line of Table 5.7 $\max \varepsilon_r^{glob}(x) = (1.79)^2 \approx 3.2$, then we took $d = 3.4$ in (5.4). Thus,

$$d = 3.4, \ \beta = 0.985,$$

where the number $\beta$ is defined in (5.35). Hence, the admissible set of parameters is:

$$\varepsilon_r(x) \in C_M = \{1 \leq \varepsilon_r(x) \leq 4\}.$$

We now give the values of the parameter $B_{\text{cut}}$ in (5.38). Let $k$ be the number of the mesh refinement. We took

$$B_{\text{cut}} := B_{\text{cut}}(k) = \begin{cases} 0.91, \text{ for } k = 1, 2, \\ 1.1 \text{ for } k = 3, \\ 2 \text{ for } k > 3. \end{cases}$$

The stopping criterion for mesh refinements was the same as the one in Sect. 5.9.4.

#### 5.9.5.1 The First Stage

Because of the above criterion, we have stopped on the third mesh refinement. The corresponding image is displayed on Fig. 5.12. Comparing with Fig. 5.8c, one can observe an improvement of the shape of the image. However, one can also see two disconnected inclusions on Fig. 5.12 instead of just one on Fig. 5.8c. In addition, the value of the refractive index is now $n = 1.59$, which is 12% less than the value of 1.79 listed in Table 5.7.

#### 5.9.5.2 The Second Stage

We know from the image of Fig. 5.8c, which is obtained by the approximately globally convergent numerical method, that we have only one inclusion rather than two disconnected as ones on Fig. 5.12. In addition, we also know from Fig. 5.8c that this inclusion is located below the small upper inclusion imaged on Fig. 5.12. Hence, we have decided to refine mesh in the intersections of two subdomains $\Omega_1, \Omega_2 \subset \Omega$. The subdomain $\Omega_1$ is defined as usual when the second mesh refinement recommendation is used:

$$\Omega_1 = \left\{ x \in \Omega : \overline{\varepsilon}_r(x) \geq 0.2 \max_{\overline{\Omega}} \overline{\varepsilon}_r(x) \right\}.$$

As to the subdomain $\Omega_2$, this is a rectangular prism whose upper boundary is slightly below the lower boundary of the small inclusion imaged on Fig. 5.12. And the lower boundary of $\Omega_2$ is slightly below the lower boundary of the larger inclusion imaged on Fig. 5.12.

Let $\Omega_3 = \Omega_1 \cap \Omega_2$. Then, our calculations show that

$$\Omega_3 = \{(x, y, z) \in [-0.6, 0.6] \times [-0.6, 0.6] \times [-1.8, -0.8]\}.$$

Thus, we refine mesh in neighborhoods of all points of the rectangular prism $\Omega_3 \subset \Omega$. The final image is displayed on Fig. 5.13. It is obtained after the third mesh refinement.

An excellent accuracy of the reconstruction of all three components for cube number 2 is evident from Fig. 5.13. These three components are location, shape, and refractive index.

### 5.9.6 Sensitivity to the Parameters α and β

We have tested the sensitivity of the image of Cube No. 2 to the choice of the regularization parameter $\alpha \in (0,1)$ in the Tikhonov functional (5.16) as well as to the choice of the parameter $\beta \in (0,1)$ on the third stage of data immersing. We have performed the following tests:

$$\beta = 0.985;\ \alpha = 0.001, 0.01, 0.1; \tag{5.40}$$

$$\beta = 0.5;\ \alpha = 0.001, 0.01, 0.1; \tag{5.41}$$

$$\beta = 0.1; \alpha = 0.001, 0.01, 0.1. \tag{5.42}$$

Results of these tests are displayed on Fig. 5.14. One can observe that, for any given value of $\beta$, the change of the regularization parameter $\alpha$ by the factor of 100 causes almost no change in imaging results. In addition, the change of the parameter $\beta$ by the factor of $1.97 = 0.985/0.5$ affects results very insignificantly. Surprisingly, even for $\beta = 0.1$, we got almost the same visual quality of images as ones for $\beta = 0.5, 0.985$. However, the value of the imaged refractive index became 1.55 instead of the correct value of 1.78.

We conclude, therefore, that our procedure is quite stable with respect to changes of parameters $\alpha$ and $\beta$.

### 5.9.7 Additional Effort for Cube Number 1

We undertook an additional effort for cube number 1 on the adaptivity stage. Recall that the adaptivity requires solutions of state and adjoint problems on each iteration. Also, it was stated in Sect. 5.5 that in the case of these experimental data, our state problem is the problem (5.11). The main new element of this additional effort is that we use in (5.10) and (5.11) a higher frequency $\omega = 14$ instead of the previous one of $\omega = 7$. This is because $\omega = 14$ corresponds to the twice smaller dimensionless wavelength $2\pi/\omega \approx 0.45$. Indeed, the dimensionless size of cube number 1 is $0.8 \times 0.8 \times 0.8$ and $0.8/0.45 \approx 1.78 > 1$. On the other hand, $2\pi/7 \approx 0.897$ and $0.8/0.897 \approx 0.89 < 1$. In other words, we had less than one dimensionless wavelength per the side of cube number 1. However, in the new test, we have almost two wavelengths are per the side of this cube. Thus, we have conjectured that this new value of $\omega = 14$ might provide an image whose quality would be better than the one on Fig. 5.11.

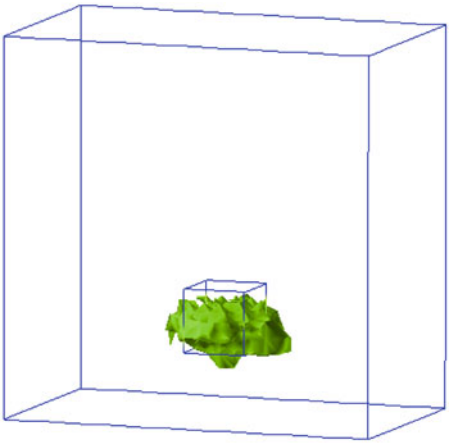

$$\varepsilon_{r,h} \approx 3.9, n_{glob} = \sqrt{\varepsilon_{r,h}} \approx 1.97$$

**Fig. 5.11** The reconstruction result for the second stage of the adaptivity for the cube number 1. *Thin lines* (*blue*) indicate the correct cubical shape. Comparison with Fig. 5.10 shows an improvement of the image. The refractive index is reconstructed accurately (Table 5.8). Source: L. Beilina and M.V. Klibanov, Reconstruction of dielectrics from experimental data via a hybrid globally convergent/adaptive inverse algorithm, *Inverse Problems*, 26, 125009, doi:10.1088/0266-5611/26/12/125009, 2010. © IOP Publishing. Reprinted with permission

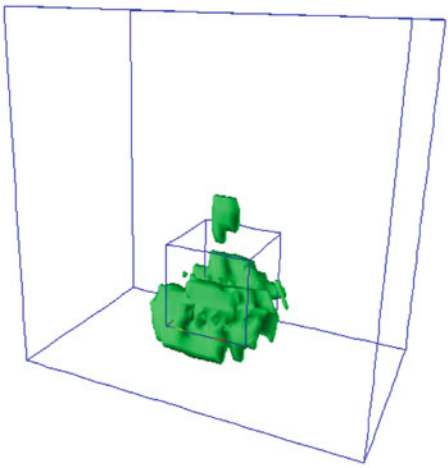

$$\varepsilon_{r,h} \approx 2.52, n_{glob} = \sqrt{\varepsilon_{r,h}} \approx 1.59$$

**Fig. 5.12** The reconstruction result for the first stage of the adaptivity for the cube number 2. Only maximal values of the imaged coefficient are shown for the third refined mesh. The shape of the final imaged coefficient is better than one on Fig. 5.9c. However, the imaged refractive index is lowered by about 19% compared with the imaged on the globally convergent stage. Source: L. Beilina and M.V. Klibanov, Reconstruction of dielectrics from experimental data via a hybrid globally convergent/adaptive inverse algorithm, *Inverse Problems*, 26, 125009, doi:10.1088/0266-5611/26/12/125009, 2010. © IOP Publishing. Reprinted with permission

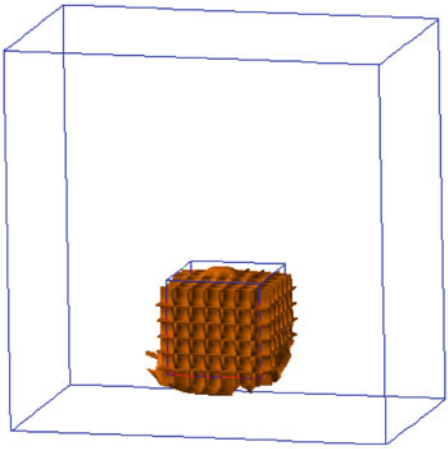


**Fig. 5.13** The final reconstruction result for the cube number 2. Only the final, third mesh refinement, is shown. The imaged coefficient $\varepsilon_r(x) = 1$ outside of these images. All three components: shape, location, and refractive index are imaged with a very good accuracy. Source: L. Beilina and M.V. Klibanov, Reconstruction of dielectrics from experimental data via a hybrid globally convergent/adaptive inverse algorithm, *Inverse Problems*, 26, 125009, doi:10.1088/0266-5611/26/12/125009, 2010. © IOP Publishing. Reprinted with permission

First, we have simulated the data for the same inclusion as cube number1 is. In other words, we took the same location and size as ones listed in Table 5.7. Also, we took $\varepsilon_r = 4$ inside this inclusion and $\varepsilon_r = 1$ everywhere else. We have applied the same procedure as above to these computationally simulated data, starting from the approximately globally convergent method. The resulting image is displayed on Fig. 5.16a. A very good accuracy of reconstruction of location, shape, and refractive index is evident from Fig. 5.16a.

Next, we have applied the entire above procedure to the experimental data for cube number 1 with the new value of $\omega = 14$ in (5.10). Figure 5.16b displays the final resulting image of cube number 1. One can observe a significant improvement compared with Fig. 5.11.

Still, the image of Fig. 5.16b is not as perfect as the one of Fig. 5.13. We attribute this to the sizes of cubes 1 and 2. Indeed, the original wavelength of the signal in the experimental data was $\lambda = 3$ centimeters (cm). Hence, since the size of the side of cube number 1 is 4 cm, then its side is $1.33\lambda$. On the other hand, the side of cube number 2 is 6 cm, which is $2\lambda$. wavelengths. We conjecture that it is this difference of sizes which led to the difference of the quality of images of these two cubes.

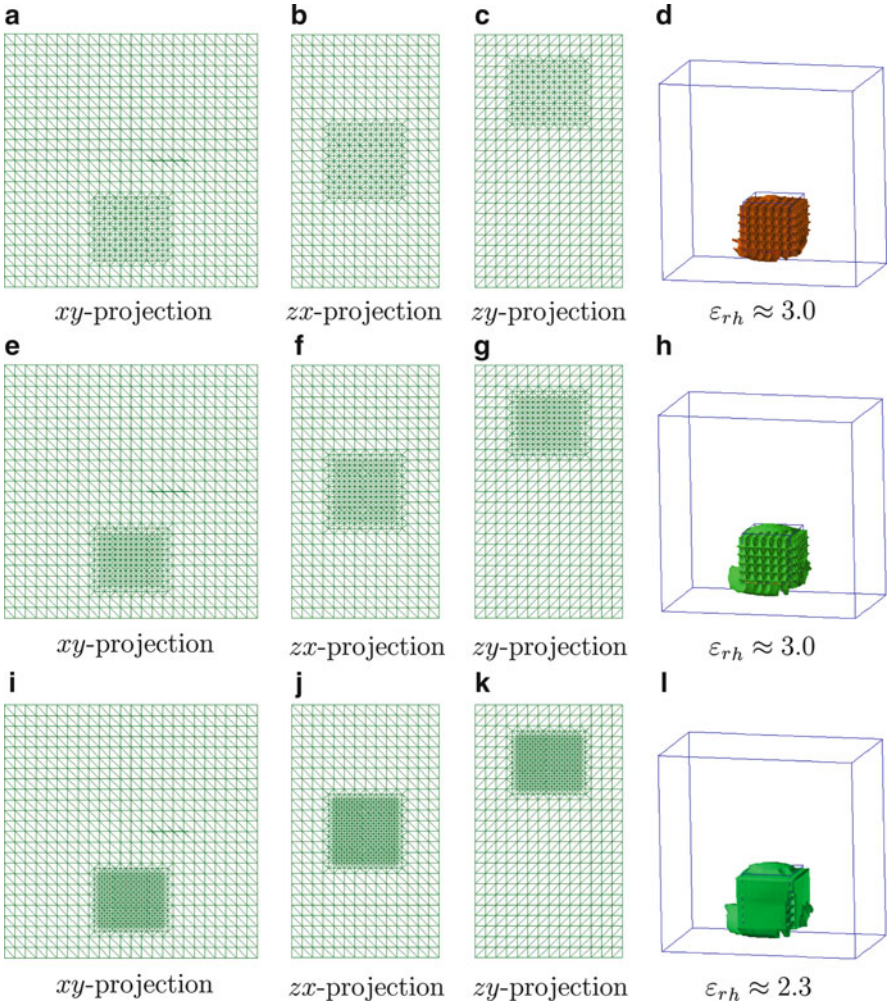


**Fig. 5.14** Adaptively refined computational meshes in different projections and reconstruction results for cube number 2 with parameters $\beta = 0.985$ and $\alpha = 0.001$. *Lines* (*blue*) indicate the correct *cubical shape*. Maximal values of the imaged coefficient are displayed. The computed value of the coefficient outside of imaged inclusions is 1. We observe that a very good reconstruction is achieved on (**d**). The image on (**d**) is the same as the image on Fig. 5.13. This image is obtained after three mesh refinements. The same stopping criterion as the one in Sects. 4.15.3 and 4.16.2 was used. Relaxation Theorems 4.9.3 and 4.11.4 help in this case. On the other hand, (**h**) shows that reconstruction is stabilized, and (**l**) shows that the image deteriorates if one uses more mesh refinements than necessary, i.e., if one ignores that stopping criterion. Thus, (**d**) is our final image. Source: L. Beilina and M.V. Klibanov, Reconstruction of dielectrics from experimental data via a hybrid globally convergent/adaptive inverse algorithm, *Inverse Problems*, 26, 125009, doi:10.1088/0266-5611/26/12/125009, 2010. 

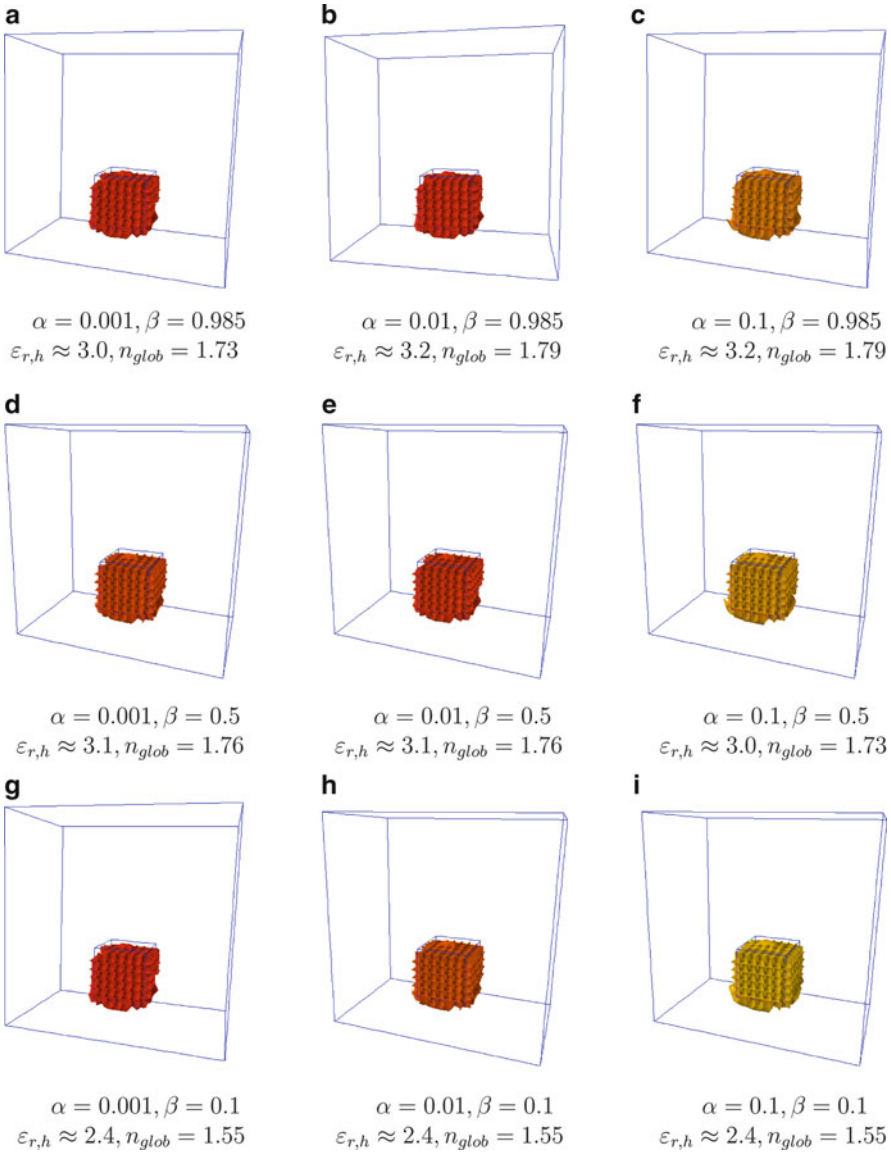


**Fig. 5.15** Final reconstruction results for cube number 2 with varying parameters $\beta$ and $\alpha$. *Lines* (*blue*) indicate the correct cubical shape. Maximal values of the imaged coefficient are displayed. The computed value of the coefficient outside of imaged inclusions is 1. Source: L. Beilina and M.V. Klibanov, Reconstruction of dielectrics from experimental data via a hybrid globally convergent/adaptive inverse algorithm, *Inverse Problems*, 26, 125009, doi:10.1088/0266-5611/26/12/125009, 2010. 

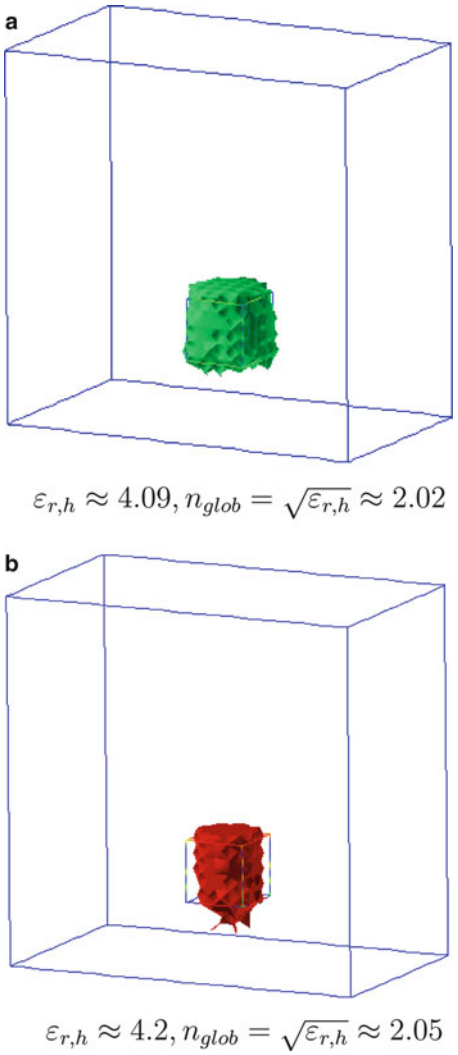


**Fig. 5.16** (**a**) The image of computationally simulated cube number 1 from computationally simulated data with $\omega = 14$ in (5.10) and (5.11). (**b**) The image of cube number 1 from experimental data with $\omega = 14$ in (5.10) and (5.11). The same imaging procedure as above was applied. Compared with Fig. 5.11, a significant improvement is observed. Still, however, the image of the shape is not as good as the one for Cube number 2 on Fig. 5.13. Source: L. Beilina and M.V. Klibanov, Reconstruction of dielectrics from experimental data via a hybrid globally convergent/adaptive inverse algorithm, *Inverse Problems*, 26, 125009, doi:10.1088/0266-5611/26/12/125009, 2010. © IOP Publishing. Reprinted with permission

## 5.10 Summary

In this chapter, we have presented our work on experimental data of [28, 109]. The main difficulty of this work was caused by a **huge discrepancy** between experimentally measured and computationally simulated data. This discrepancy is not only due to the noise component, which is always present in any experimental data, but also due to a highly oscillatory behavior of experimentally measured curves, even for the case of the free space. On the other hand, computational simulations for the free space case do not show high oscillations. Thus, it is unclear

what kind of a PDE, if any, governs this process. We attribute this discrepancy to very small times at which experimental data were collected. Indeed, the time step between two consecutive readings was only $20\,\text{ps} = 2 \times 10^{-11}\,\text{s}$.

We have modeled this process by a single hyperbolic PDE (5.1), which is the same as (2.1). The Maxwell's system was not used. We believe that modeling by this system might lead to a better accuracy of results. Still, however, an analog of the above data pre-processing procedure should be used. Since only a single component of the electric field was measured and since the approximately globally convergent numerical method is not yet developed for CIPs for the Maxwell's system, then the above question should be left for future studies.

To handle the above huge discrepancy, a **crucial** step was a **radically new** data pre-processing procedure. This procedure consists in immersing the data in the mathematical model we are working with. We point out that the immersing procedure was **unbiased**. This is because our approximately globally convergent algorithm has worked with the most challenging case of **blind** experimental data, i.e., we did not know the answer in advance. The immersing procedure makes the data suitable to work with. This procedure consists of three stages. First two immersing stages were applied to work with the algorithm of Sect. 2.6.1. And the third stage was applied to make the data suitable for the adaptivity technique.

We had at least five (5) sources of error:

1. The natural noise in the experimental data.
2. The modeling noise, since it was unclear from the data analysis what kind of PDE, if any, governs the process.
3. The data pre-processing has contributed even more to the modeling noise.
4. In our theory, the coefficient $\varepsilon_r(x)$ should be sufficiently smooth. However, this function obviously had a discontinuity at the inclusion/medium interface.
5. The Maxwell's system was not used.

Nevertheless, we have consistently obtained an excellent accuracy of the reconstruction of both locations and refractive indices of dielectric inclusions in blind testing by the first stage of our two-stage numerical procedure. We point out that when applying the algorithm of Sect. 2.6.1, we were unbiased; see beginning of Sect. 5.7. The second stage has also resulted in an excellent reconstruction accuracy of locations and refractive indices of both cubes. In addition, the second stage has led to reconstructions of shapes of these cubes. The shape reconstruction accuracy was excellent for cube number 2, and it was very good for cube number 1. We conjecture that this difference of qualities is due to the difference of sizes of those cubes versus the wavelength $\lambda$ of the EM wave we were operating with. Indeed, the size of the side of for 1 was $1.33\lambda$ versus to $2\lambda$ of cube number 2.

With reference to the two-stage numerical procedure, we have shown how important it is to use the approximately globally convergent algorithm on the first stage. Indeed, first, we have demonstrated that a modified gradient method of the minimization of the Tikhonov functional does not produce meaningful results, if it is taken alone, i.e., without the first stage algorithm of Sect. 2.6.1. Next, it is important for the third stage of data immersing to use the result obtained by the algorithm of

Sect. 2.6.1. In addition, we have shown that our adaptivity technique, being applied to these experimental data, is very stable with respect to the large changes of two key parameters: the regularization parameter $\alpha$ of the Tikhonov functional and the parameter $\beta$ of the third stage of data immersing.

In summary, we repeat one thought of Sect. 5.1. Namely, it is quite surprising that, despite all these sources of error and especially despite the abovementioned huge misfit between experimentally measured and computationally simulated data, such a very good reconstruction accuracy was consistently observed. Finally, another interesting feature of results of this chapter is that this accuracy was obtained for the case when measurements were taken for a narrow view angle; see Fig. 5.1. We believe, therefore, that these results indicate a good degree of robustness of our algorithms. Finally, we believe that these results completely validate both first and second approximate mathematical models.